Computer Physics Communications 292 (2023) 108885

Contents lists available at ScienceDirect

Computer Physics Communications

journal homepage: www.elsevier.com/locate/cpc

Computer Programs in Physics

NEMOH: Open-source boundary element solver for computation of first- and second-order hydrodynamic loads in the frequency domain ☆,☆☆

Ruddy Kurnia, Guillaume Ducrozet *

Nantes Université, Ecole Centrale Nantes, CNRS, LHEEA, UMR 6598, F-44000 Nantes, France

ARTICLE INFO

Article history:
Received 24 February 2023
Received in revised form 24 July 2023
Accepted 31 July 2023
Available online 9 August 2023

Keywords:
Boundary element method
Potential flow
Frequency domain
Fluid-structure interactions
Quadratic transfer functions
Second-order hydrodynamic loads

ABSTRACT

NEMOH is developed to solve potential flow problems using the boundary element method for computing wave loads on offshore structures. The solver solves the first-order problem in the frequency domain. An extended module enables computation of the second-order loads on a structure in bi-chromatic bi-directional waves. NEMOH is released as open-source, developed, and distributed under the terms of GNU General Public License (GPLv3). Along with the source code, a user manual is available which facilitates the compilation and execution of the source files. In this new release, NEMOH v3.0 has new features; irregular frequencies removal method, new linear system solvers for enhancing computational efficiency, and a new module for computing the full quadratic transfer function (QTF) of drift forces. Verification cases are shown for a truncated cylinder, a truncated cylinder with a thin heave plate, a spar buoy platform (SOFTWIND), and a semi-submersible platform (OC4). The results are compared with reference data from commercial software, WAMIT, DIODORE, and HYDROSTAR, and the comparison showed that NEMOH v3.0 is accurate and efficient.

Program summary

Program Title: NEMOH
CPC Library link to program files: https://doi.org/10.17632/k9v4hjb5xj.1
Developer's repository link: https://gitlab.com/lheea/Nemoh
Code Ocean capsule: https://codeocean.com/capsule/9256007
Licensing provisions: GPLv3
Programming language: Fortran
External libraries and programs: BLAS [1], LAPACK [2]
Nature of problem: NEMOH solves the potential flow problems of diffraction and radiation in wave-structure interactions. Typical use is the estimation of the dynamic response of floating structures, e.g. floating offshore wind turbine platforms, or wave-energy converters.
Solution method: The linear potential flow problems, diffraction and radiation, are expressed in the boundary integral of the source distribution formulation. The equations are solved in the frequency domain and implemented using the boundary element method with quadrilateral panels. The source distribution on the body panels is obtained by solving the linear system. The hydrodynamic coefficients are computed with the known source distribution. The second-order potential flow problem is not solved directly; the Green formulation is used with an assisting function which is the instantaneous radiation potential, that allows the computation of second-order force for given first-order hydrodynamic quantities.
Additional comments including restrictions and unusual features:

- The previous version, NEMOH v2.0 [3], was available only for computing first-order hydrodynamic coefficients without the irregular frequency removal method. NEMOH v3.0 has new features, the extended boundary integral method is implemented for removing the irregular frequencies, new

☆ The review of this paper was arranged by Prof. W. Jong.

☆☆ This paper and its associated computer program are available via the Computer Physics Communications homepage on ScienceDirect (http://www.sciencedirect.com/science/journal/00104655).

* Corresponding author.
E-mail address: guillaume.ducrozet@ec-nantes.fr (G. Ducrozet).

https://doi.org/10.1016/j.cpc.2023.108885
0010-4655/© 2023 The Author(s). Published by Elsevier B.V. This is an open access article under the CC BY-NC-ND license (http://creativecommons.org/licenses/by-nc-nd/4.0/).

linear system solvers are added for enhancing computational efficiency, and a new module is added for computing second-order wave loads. NEMOH v3.0 has better accuracy than v2.0 due to finer interpolation points of the free-surface Green function and a better integration method for constructing the influence coefficients.

- For the free-surface piercing bodies problem, it is known that non-unique solutions exist in the boundary integral equation at certain frequencies. In NEMOH, the extended boundary integral equation is applied to remove the irregular frequencies by providing the lid panels on the body waterplane. The second-order loads require the computation of the free-surface forcing terms in the integral forms. These free-surface integrals are essential for the sum-frequency wave loads but may be negligible in the difference-frequency loads. For now, it is suggested not to apply the lid panels when the free-surface integrals are computed.

References

[1] https://netlib.org/blas/.
[2] https://netlib.org/lapack/.
[3] A. Babarit, G. Delhommeau, Theoretical and numerical aspects of the open source BEM solver NEMOH, Proceedings of the 11th European Wave and Tidal Energy Conference, 2015.

© 2023 The Author(s). Published by Elsevier B.V. This is an open access article under the CC BY-NC-ND license (http://creativecommons.org/licenses/by-nc-nd/4.0/).

1. Introduction

Accurate and efficient computation of nonlinear wave loads on a floating structure is of particular concern in ocean engineering. In the design of floating structures, e.g., wave energy converter devices or floating wind turbine platforms, nonlinear wave-structure interactions have to be taken into account. This concerns, for instance, avoiding uncontrolled motion of the floating structure due to resonance phenomena, such as slow drift or springing, at the natural frequencies of the floating structure with the presence of moorings [1–3]. In this respect, potential flow codes, such as NEMOH, could play a role in the hydrodynamic design of the floating structure.

NEMOH, developed at Ecole Centrale de Nantes, was the first open-source potential flow boundary element solver [4]. Since its first release in 2014, the software has been widely used for ocean engineering applications, such as the design of wave-energy converter devices [5–8], floating offshore wind turbine platforms [9,10] and hybrid wind-wave energy converter devices [11,12]. The hydrodynamic database from NEMOH is often used as an input for time domain body dynamic solvers as reported in [13]. NEMOH can compute the hydrodynamic interaction of multi-bodies and can be coupled with a wave propagation model for studying the far-field effect of the interaction as reported in [14] for wave energy converter arrays.

Performance of the previous NEMOH version (v2.0) has been reported in comparison studies against the commercial software WAMIT [15] in [5,7], and against the open-source software HAMS [16] in [7]. In the previous release version, NEMOH v2.0 was available only for computing first-order hydrodynamic coefficients without the irregular frequency removal method. The studies reported that NEMOH had good accuracy in most applications with limitations in computational cost, irregular frequencies, and documentation. NEMOH v2.0 had poor accuracy when dealing with a thin structure, i.e. heave plate, due to the accuracy of the look-up table and the interpolation method on the free-surface Green function as noted in [4] and reported in [7].

This paper reports the release of NEMOH v3.0. In this version, an extended boundary integral method for irregular frequency removal is implemented, new linear system solvers are added to enhance the computational efficiency, and an extended module to compute second-order wave load quadratic transfer functions (QTFs) is also available. NEMOH v3.0 has better accuracy than v2.0 with finer interpolation points of the free surface Green function computation and the influence coefficients are now obtained by applying the Gauss-quadrature integration method. As in the previous version, NEMOH v3.0 can deal with multi-bodies interaction. NEMOH v3.0 can be extended for solving diffraction and radiation problems of deflection modes of a flexible body. This new feature is expected to be added in the updated v3.0 version.

The QTF module in NEMOH v3.0 is a new feature and probably the only open-source software that provides the module. The first development of the QTF module was reported in [17]. Extensive verification of recent developments of the QTF module, against the commercial software developed by Bureau Veritas HYDROSTAR [18], for uni-directional QTFs, was reported in [19] and for bi-directional QTFs in [20].

NEMOH software is available for downloading and contributions on the Gitlab platform [21]. The code is developed and redistributed under the terms of the GNU General Public License as published by the Free Software Foundation. Along with the source code, documentation that describes the compilation and execution of the source files is also distributed.

Four floating platforms are considered for verification cases; a truncated cylinder, a truncated cylinder with a thin heave plate, a spar-buoy (SOFTWIND) and a semi-submersible (OC4). The NEMOH results are compared with WAMIT [15], HYDROSTAR [18] and DIODORE [22] software.

This paper is organized as follows. Section 2 describes theoretical and numerical aspects of the open-source NEMOH. Section 3 describes program documentation of the source files, compilation, execution of the codes, input/output files, and test cases. The verification cases with the comparison results are discussed in Section 4. The conclusions are provided in Section 5.

2. NEMOH

In this section, the theoretical and numerical aspects of NEMOH are described.

2.1. Notation

As sketched in Fig. 1, we consider a fluid domain with the Cartesian coordinates $\boldsymbol{x} = (\vec{x}, z)$ with $\vec{x} = (x, y)$ the horizontal coordinates perpendicular to the z axis in the opposite direction of gravity $\boldsymbol{g}$. The free-surface boundary S_F is defined by the free surface elevation at time t denoted as $z = \eta(\vec{x}, t)$ with respect to the mean water level at $z = 0$, S_{F_0}. The fluid velocity potential is denoted as $\Phi(\boldsymbol{x}, t)$ with $\boldsymbol{x}$ in the fluid domain V_Ω.

The rigid floating body has 6 degrees of freedom (DOF), $\boldsymbol{\xi} = (\boldsymbol{X}, \boldsymbol{\theta})$ where the positions, $\boldsymbol{X} = (X, Y, Z)$ and the orientations, $\boldsymbol{\theta} = (\theta_1, \theta_2, \theta_3)$ are determined at the center of gravity (COG), $\boldsymbol{x}_{COG}$.

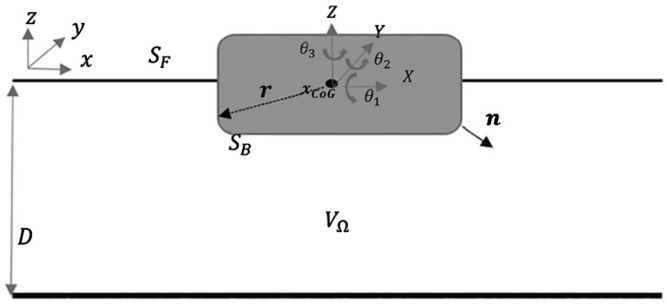

Fig. 1. Sketch of the system.

Displacement of points at the hull is specified by a body of vector $\boldsymbol{r}$ with respect to the COG as $\boldsymbol{\mathcal{X}} = \boldsymbol{X} + R(\boldsymbol{r})$. R is a rotation operator where $R(\boldsymbol{r}) = \boldsymbol{\theta} \times \boldsymbol{r}$. The velocity of the points at the hull is expressed as $\dot{\boldsymbol{\mathcal{X}}}$.

On the body hull S_B, the wetted part is defined as a function $z = \zeta(\vec{x}, t)$. The normalized normal vector is defined as directed toward the fluid domain, $\boldsymbol{n} = -\boldsymbol{N}/|\boldsymbol{N}|$ with $\boldsymbol{N} = (-\nabla_2\zeta, 1)$ where ∇_2 is the two-dimensional gradient in $\vec{x}$. Then the six-dimensional generalized normal vector is defined as $\boldsymbol{\nu} = (\boldsymbol{n}, \boldsymbol{r} \times \boldsymbol{n})^T$, with $()^T$ defining the matrix transpose operator. The normal vectors on the body at the mean position, S_{B_0} are expressed as $\boldsymbol{\nu}_0$ and $\boldsymbol{n}_0$.

2.2. Hydrodynamic problem

In potential flow theory, the fluid is assumed to be inviscid and the flow is irrotational, $\nabla \times \boldsymbol{U} = 0$; the fluid velocity $\boldsymbol{U}$ can then be written as $\boldsymbol{U} = \nabla\Phi$ with Φ the velocity potential. The fluid in the interior domain, V_Ω, is incompressible so that this velocity potential satisfies the Laplace equation.

This fluid velocity potential has to satisfy a set of boundary conditions: first, free surface conditions on S_F; second, the diffraction and radiation conditions on the body hull, S_B; third, the impermeable condition at the bottom, $z = -D$, and lastly, the radiation wave condition at the far field, $|\vec{x}| \to \infty$.

The potential flow problem can be truncated in terms of nonlinearity by applying the perturbation series. These perturbation series are applied to the fluid potential, the wave elevation, the body displacement, the rotation operator, and the normal vector on the body hull. The fluid potential on the free surface and on the body hull is approximated using the Taylor series at the mean water level $z = 0$ and at the mean body hull S_{B_0}, respectively. The hydrodynamic problem can then be reformulated at the first order, $m = 1$, and at the second order of nonlinearity, $m = 2$, as

$$\begin{cases} \nabla^2\Phi^{(m)}(\boldsymbol{x}, t) = 0 & \boldsymbol{x} \in V_\Omega \\ \partial_t^2\Phi^{(m)} + g\partial_z\Phi^{(m)} = Q_F^{(m)} & \boldsymbol{x} \in S_{F_0} \\ \partial_n\Phi^{(m)} = \dot{\boldsymbol{\mathcal{X}}}_B^{(m)} \cdot \boldsymbol{n}_0 + Q_B^{(m)} & \boldsymbol{x} \in S_{B_0} \\ \partial_z\Phi^{(m)}(\boldsymbol{x}) = 0 & \text{at } z = -D \\ \lim(\Phi^{(m)} - \Phi_I^{(m)}) = 0 & \text{for } x^2 + y^2 \to \infty, \end{cases} \tag{1}$$

where the free surface forcing term, $Q_F^{(m)}$, and the body forcing term, $Q_B^{(m)}$, are zero for $m = 1$, and for $m = 2$ are given by

$$Q_F^{(2)} = -2\nabla\Phi^{(1)} \cdot \partial_t\nabla\Phi^{(1)} + \frac{1}{g}\partial_t\Phi^{(1)}\partial_z\left[\partial_{tt}\Phi^{(1)} + g\partial_z\Phi^{(1)}\right]\Big|_{z=0} \tag{2}$$

$$Q_B^{(2)} = \left[\dot{\boldsymbol{\mathcal{X}}}^{(1)} - \nabla\Phi^{(1)}\right] \cdot R^{(1)}(\boldsymbol{n}_0) - \left[\left(\boldsymbol{\mathcal{X}}^{(1)} \cdot \nabla\right)\nabla\Phi^{(1)}\right] \cdot \boldsymbol{n}_0\Big|_{S_{B_0}}. \tag{3}$$

The fluid potential is composed of the incident wave potential, $\Phi_I^{(m)}$, and the perturbed potential, $\Phi_P^{(m)}$, as $\Phi^{(m)} = \Phi_I^{(m)} + \Phi_P^{(m)}$. The perturbed potential is a sum of the diffraction potential and the radiation potential, $\Phi_P^{(m)} = \Phi_D^{(m)} + \Phi_R^{(m)}$. The radiation potential is defined as

$$\Phi_R^{(m)} = \dot{\boldsymbol{\xi}}^{(m)} \cdot \boldsymbol{\psi} \tag{4}$$

where the instantaneous radiation potential vector, $\boldsymbol{\psi} = (\Phi_{R_1}, \Phi_{R_2}, \cdots, \Phi_{R_6})$.

In NEMOH, the first-order hydrodynamic problem is formulated in the source distribution boundary integral equations and is solved using a panel method as in [4] and is described in Section 2.3.

The second-order hydrodynamic problem is not solved directly, but the second-order force for sum- and difference-frequencies can be calculated using the indirect method as in [23,24]. This is described in Section 2.4.

2.3. First-order problem

This section describes the definition of the incident wave potential, the boundary integral equation for solving the first-order problem of Eq. (1), hydrodynamic forces, response amplitude operator of motion, and numerical implementations.

2.3.1. Incident wave potential

The first-order harmonic incident potential is defined as

$$\Phi_I^{(1)}(\boldsymbol{x}, t) = Re\left\{\Phi_I^{(1)}(\boldsymbol{x})e^{-i\omega t}\right\}, \tag{5}$$

$$\Phi_I^{(1)}(\boldsymbol{x}) = -i\frac{ag}{\omega}\mathcal{Z}(k, D, z)e^{i\vec{k}\cdot\vec{x}}, \tag{6}$$

with wave amplitude a, the radial frequency ω, the wave propagation direction β that is the angle from the positive x-axis, the wave number vector $\vec{k} = k(\cos\beta, \sin\beta)$, and the water depth D. The Airy vertical profile is defined as $\mathcal{Z}(k, D, z) = \frac{\cosh(k(D+z))}{\cosh kD}$. The wave frequency and the wave number $k = \left|\vec{k}\right|$ are related with the linear dispersion relation as

$$\omega = \Omega(k, D) = \sqrt{gk\tanh kD}. \tag{7}$$

2.3.2. Boundary integral equation

The three-dimensional linear potential flow problem around an arbitrary body condition, Eq. (1), is reformulated in the Boundary Integral Equation (BIE) and transformed into the two-dimensional problem of the source distribution, σ, on the body surface, S_B, using Green's second identity and the appropriate Green function, $G(\boldsymbol{x}, \boldsymbol{x}')$. The Green function is based on Delhommeau's formulation and is available for finite and infinite water-depth, see [25,4].

The source distribution depends on the boundary condition problem considered. For each frequency and wave direction, the diffraction source distribution, $\sigma_D(\boldsymbol{x})$, depends on the position of the panels while the radiation source distribution, $\sigma_{R_j}(\boldsymbol{x})$, depends on the position of the panels and the considered degree of freedom j. Then, the BIE for $\boldsymbol{x} \in S_B$ with flow points $\boldsymbol{x}$ and source points $\boldsymbol{x}'$, is expressed as

$$\frac{1}{2}\sigma_{D,R_j}(\boldsymbol{x}) - \frac{1}{4\pi}\iint_{S_B}\partial_n G(\boldsymbol{x}, \boldsymbol{x}')\sigma_{D,R_j}(\boldsymbol{x}')dS' = \mathcal{N}_{D,R_j}(\boldsymbol{x}), \tag{8}$$

where $\mathcal{N}(\boldsymbol{x})$ is the body normal condition. The diffraction normal condition is defined as $\mathcal{N}_D(\boldsymbol{x}) = -\partial_n\Phi_I^{(1)}(\boldsymbol{x})$, and the normalized radiation condition, $\mathcal{N}_{R_j}(\boldsymbol{x}) = \partial_n\Phi_{R_j}(\boldsymbol{x}) = \nu_{0_j}$. This leads to a linear system with the known influence matrix and the unknown source distribution.

After the linear system has been solved and the source distribution obtained, the diffraction potential, $\Phi_D^{(1)}$, the normalized radiation potential vector component j, Φ_{R_j} and the corresponding velocities are then computed as follows, for the flow points in the fluid domain $\boldsymbol{x} \in S_B \cup V_{\Omega_F}$,

$$\Phi_{D,R_j}^{(1)}(\boldsymbol{x}) = -\frac{1}{4\pi} \iint_{S_B} G(\boldsymbol{x},\boldsymbol{x}')\sigma_{D,R_j}(\boldsymbol{x}')dS' \tag{9}$$

$$\partial_{\boldsymbol{x}}\Phi_{D,R_j}^{(1)}(\boldsymbol{x}) = \frac{1}{2}\sigma_{D,R_j}(\boldsymbol{x})\boldsymbol{n}\delta_{\boldsymbol{x}\boldsymbol{x}'} - \frac{1}{4\pi} \iint_{S_B} \partial_{\boldsymbol{x}} G(\boldsymbol{x},\boldsymbol{x}')\sigma_{D,R_j}(\boldsymbol{x}')dS' \tag{10}$$

where the Kronecker delta $\delta_{\boldsymbol{x}\boldsymbol{x}'} = 1$ for $\boldsymbol{x} = \boldsymbol{x}'$, and $\delta_{\boldsymbol{x}\boldsymbol{x}'} = 0$ otherwise.

2.3.3. Hydrodynamic forces

The first-order excitation force, $\boldsymbol{F}_{exc}^{(1)}$, is defined as

$$\boldsymbol{F}_{exc}^{(1)} = \rho \iint_{S_B} -i\omega\left[\Phi_I^{(1)} + \Phi_D^{(1)}\right]\boldsymbol{\nu}_0 dS. \tag{11}$$

The radiation force is defined, with the radiation potential in Eq. (4), as

$$\boldsymbol{F}_{rad}^{(1)} = \rho \iint_{S_B} -i\omega\Phi_R^{(1)}\boldsymbol{\nu}_0 dS = [\boldsymbol{M}^a]\ddot{\boldsymbol{\xi}} + [\boldsymbol{B}]\dot{\boldsymbol{\xi}}. \tag{12}$$

The added mass matrix, $[\boldsymbol{M}^a]$, and the damping coefficient matrix, $[\boldsymbol{B}]$, components are defined as

$$M_{ij}^a = -\rho \iint_{S_B} \nu_{0_i} Re\left\{\Phi_{R_j}\right\} dS \tag{13}$$

$$B_{ij} = -\rho\omega \iint_{S_B} \nu_{0_i} Im\left\{\Phi_{R_j}\right\} dS. \tag{14}$$

2.3.4. Response amplitude operator of motion

The Response Amplitude Operator (RAO) is obtained by solving the following equation of motion

$$\left[-[\boldsymbol{M} + \boldsymbol{M}^a(\omega)]\omega^2 - i\omega[\boldsymbol{B}(\omega) + \boldsymbol{B}_{add}] + [\boldsymbol{K}_h + \boldsymbol{K}_M]\right]\boldsymbol{\xi}(\omega) = \boldsymbol{F}_{exc}(\omega) \tag{15}$$

where $[\boldsymbol{M}], [\boldsymbol{K}_h]$ are the matrices of the mass-inertia and the hydrostatic stiffness, respectively. The additional damping and stiffness matrices, e.g. due to the mooring line, the power take-off model of WECs, may be specified in $[\boldsymbol{B}_{add}]$ and $[\boldsymbol{K}_M]$, respectively.

2.3.5. Numerical methods

The boundary integral in Eq. (8) is discretized using the constant panel method with a quadrilateral mesh. The mesh is user-specified with the normal direction toward the fluid. It is suggested that at least 15 panels per wavelength should be used for horizontal discretization. The mesh needs to be defined only on the wetted part of the body hull. Body panels with small angles, high length and width ratio, and close to the free surface have to be avoided. NEMOH checks only the area of panels and gives a warning if the area is smaller than $< 10^{-7}m^2$.

After the body hull has been discretized with the panels, the influence matrix, in the BIE Eq. (8), is constructed with the Green function, [25], and implemented as in [4]. The free surface part of the Green function (the one involving the integration over the Fourier polar coordinate θ) may be written as a function of a few functions depending on two non-dimensional variables. For reasons of computational efficiency, the values are tabulated with the discretized non-dimensional variables of $\omega^2 r/g \in [0, 100]$ with 676 points in a constant scale and $\omega^2(z+z')/g \in [-251, -1.6\,10^{-6}]$ with 130 points in logarithmic scale. A polynomial surface interpolation with the 5^{th} order Lagrange formula is used to interpolate any values in the specified interval.

The source distributions on body panels are then obtained after solving the corresponding linear system. The linear system is solved using a user-chosen solver among the available ones, *i.e.*, Gauss elimination, LU-decomposition, and GMRES-iterative solvers [26]. GMRES solver is effective for a large system with a number of panels larger than 3000. If the convergence of the specified threshold is not achieved in the GMRES solvers, the solver will be switched to LU-decomposition automatically to ensure the solution is obtained. For computation with fewer panels, the LU-decomposition solver is the best choice.

It is known that the boundary integral equation for the free-surface piercing bodies problem excites irregularities of the solution at certain frequencies. An irregular frequency removal (IRR) method has to be applied to remove the irregularities. In NEMOH, the IRR method is activated by the user providing the body lid panels at the waterplane $z = 0$. Then, the extended boundary integral equation is solved following [4,27]. As in [27], the lid panels at $z = 0$ are shifted to $z = -\epsilon d_B$ in order to avoid singularity in the free-surface Green function. The user specifies the ϵ parameter, the default value is 0.01 in `input_solver.txt`; d_B is computed by the software as a maximum horizontal distance of points on the body. A zero normal condition is applied at the lid panels, resulting in the irregular frequencies being removed or shifted to higher frequencies. The maximum threshold for shifting z value can be estimated as in [27] based on the fact that the first irregular frequency of the general body shape is higher than the first irregular frequency of an equivalent rectangular barge surrounding the body.

2.4. Second-order wave loads

The potential flow problem, Eq. (1), is truncated for the first-order and the second-order problems by applying a perturbation series, as shown in [24,19,20]. This leads to the truncated hydrodynamic pressure and then to the truncated excitation forces. The first-order excitation force is defined in Eq. (11). The second-order excitation force is composed of the quadratic part and the potential part. The quadratic part can be computed directly based on a quadratic operation of the first-order variables. The potential parts of diffraction force can be computed using the indirect method, [23,24], without knowing the second-order diffraction potential. The diffraction force is reformulated in the Green formulation with an assisting function, which is the normalized radiation potential. The diffraction force is then composed of the body forcing integral and the free-surface integrals. An explicit formulation of the force is given in Sections 2.4.1 and 2.4.2 for the sum- and difference-frequencies Froude-Krylov force and excitation force, respectively.

2.4.1. Sum- and difference-frequencies Froude-Krylov force

Bi-chromatic, bi-directional wave propagation with two radial frequencies ω_j, with $j = 1$ and 2, wave number vectors $\vec{k}_j = (k_j \cos\beta_j, k_j \sin\beta_j)$, is described by the Airy potential as

$$\Phi_I(\boldsymbol{x}, t) = Re\left\{\Phi_{I_1}(\boldsymbol{x})e^{-i\omega_1 t} + \Phi_{I_2}(\boldsymbol{x})e^{-i\omega_2 t}\right\} \tag{16}$$

$$\Phi_{I_j}(\boldsymbol{x}) = -i\frac{a_j g}{\omega}\mathcal{Z}(k_j, D, z)e^{i\vec{k}_j\cdot\vec{x}}.$$

The product of two biharmonic functions is composed of the double frequency terms, the constant terms, the difference-frequency terms, and the sum frequency terms. The difference-

and sum-frequencies incident potentials are then obtained by applying the product identity of two bi-chromatic functions involving the Airy potential, Eq. (16), in the evaluation of the free surface forcing terms, Eq. (2), [19]. The incident potentials are then expressed, with $\omega^{\pm} = \omega_1 \pm \omega_2$, $\vec{\kappa}^{\pm} = \vec{k}_1 \pm \vec{k}_2$, $|\vec{\kappa}^{\pm}| = \sqrt{k_1^2 + k_2^2 \pm 2k_1k_2\cos(\beta_1 - \beta_2)}$, $\varkappa_j = \frac{\Omega^2(k_j,D)}{g}$ and the complex conjugate operator applied to a complex variable, i.e. γ as $\gamma^{\mathcal{C}_-} = \gamma^*$ and $\gamma^{\mathcal{C}_+} = \gamma$, as

$$\Phi_I^{(2)\pm}(\boldsymbol{x},t) = Re\left\{\Phi_{I_1}^{(2)\pm}(\boldsymbol{x})e^{-i\omega^{\pm}t}\right\} \tag{17}$$

$$\Phi_{I_1}^{(2)\pm}(\boldsymbol{x}) = \frac{ia_1a_2^{\mathcal{C}_\pm}g^2e^{i\vec{\kappa}^{\pm}\cdot\vec{x}}\mathcal{Z}(|\vec{\kappa}^{\pm}|,D,z)}{-(\omega^{\pm})^2 + \Omega^2(|\vec{\kappa}^{\pm}|,D)} \left[\frac{\omega^{\pm}}{\omega_1\omega_2}\left(\vec{k}_1\cdot\vec{k}_2 \mp \varkappa_1\varkappa_2\right) + \frac{1}{2}\left[\frac{k_1^2-\varkappa_1^2}{\omega_1} \pm \frac{k_2^2-\varkappa_2^2}{\omega_2}\right]\right].$$

The sum- and difference-frequencies Froude-Krylov force can be computed directly with the incoming potential given in Eq. (17) as

$$\boldsymbol{F}_{H_I}^{(2)\pm} = -i\omega^{\pm}\rho \iint_{S_{B_0}} \Phi_I^{(2)\pm}\boldsymbol{\nu}_0 dS. \tag{18}$$

2.4.2. Sum- and difference-frequencies excitation force

The second-order excitation force is expressed as

$$\boldsymbol{F}_{exc}^{(2)} = \boldsymbol{F}_{exc_1}^{(2)} + \boldsymbol{F}_{exc_2}^{(2)} \tag{19}$$

where $\boldsymbol{F}_{exc_1}^{(2)}$ and $\boldsymbol{F}_{exc_2}^{(2)}$ are the quadratic and the potential terms of the excitation force.

The quadratic part of the sum- and difference-frequencies excitation forces, with the quadratic transfer functions (QTFs), $\boldsymbol{T}_{F_Q}(\beta_1,\beta_2,\omega_1,\omega_2)$, is given as follows

$$\boldsymbol{F}_{exc_1}^{(2)} = Re\left\{\boldsymbol{T}_{F_Q}^{-}a_1a_2^*e^{-i(\omega_1-\omega_2)t}\right\} + Re\left\{\boldsymbol{T}_{F_Q}^{+}a_1a_2e^{-i(\omega_1+\omega_2)t}\right\},$$

$$\boldsymbol{T}_{F_Q}^{\pm} = \left[\boldsymbol{F}_{11}^{\pm} + \boldsymbol{F}_{12}^{\pm} + \boldsymbol{F}_{13}^{\pm} + \boldsymbol{F}_{14}^{\pm}\right]/a_1a_2^{\mathcal{C}_\pm} \tag{20}$$

where $\boldsymbol{F}_{11}^{\pm}$, $\boldsymbol{F}_{12}^{\pm}$, $\boldsymbol{F}_{13}^{\pm}$ and $\boldsymbol{F}_{14}^{\pm}$ are defined as

$$\boldsymbol{F}_{11}^{\pm} = -\frac{\rho g}{2}\int_{\Gamma_0}\left[\eta_1^{(1)} - \zeta_{wl_1}^{(1)}\right]\left[\eta_2^{(1)} - \zeta_{wl_2}^{(1)}\right]^{\mathcal{C}_\pm}\boldsymbol{\nu}_0\, d\Gamma \tag{21}$$

$$\boldsymbol{F}_{12}^{\pm} = \frac{\rho}{2}\iint_{S_{B_0}}\left[\nabla\Phi_1^{(1)}\cdot\nabla\Phi_2^{(1)\mathcal{C}_\pm}\right]\boldsymbol{\nu}_0 dS$$

$$\boldsymbol{F}_{13}^{\pm} = \frac{\rho}{2}\iint_{S_{B_0}}\left[\boldsymbol{\mathcal{X}}_1^{(1)}\cdot\left(-i\omega_2\nabla\Phi_2^{(1)}\right)^{\mathcal{C}_\pm} - \boldsymbol{\mathcal{X}}_2^{(1)\mathcal{C}_\pm}\cdot i\omega_1\nabla\Phi_1^{(1)}\right]\boldsymbol{\nu}_0 dS$$

$$\boldsymbol{F}_{14}^{\pm} = \frac{1}{2}\left[R_1^{(1)}\left(\boldsymbol{F}_{I_2}^{(1)\mathcal{C}_\pm}\right) + R_2^{(1)\mathcal{C}_\pm}\left(\boldsymbol{F}_{I_1}^{(1)}\right)\right].$$

where Γ_0 is the mean waterline, $\eta^{(1)} = -\partial_t\Phi^{(1)}/g$ is the free-surface elevation, $\zeta_{wl}^{(1)} = \boldsymbol{\mathcal{X}}^{(1)}(\boldsymbol{x}_{wl})\cdot\boldsymbol{e}_3$ with the unit vector $\boldsymbol{e}_3 = (0,0,1)$ is the instantaneous waterline, and $\boldsymbol{F}_I$ is the inertia force. The lower index of the variables on the right-hand side denotes the frequency index, i.e. $\eta_1^{(1)} = \eta^{(1)}(\omega_1)$.

The quadratic part depends only on the first-order quantities which are the first-order solution obtained in NEMOH. The first contribution is due to the free surface elevation over the waterline. The second contribution is due to the quadratic potential gradient of the Bernoulli pressure equation over the body hull. The third contribution is due to the product of body displacement and first-order pressure gradient over the body hull. The last contribution is due to the first-order rotation operator applied to the first-order inertia force.

As mentioned earlier that the potential part of the second-order diffraction force is obtained using the indirect method. The diffraction problem that satisfies the boundary value problem in Eq. (17) is reformulated in the boundary integral equations using the Green-Gauss theorem with an assisting function which is the normalized radiation potential. In the boundary integrals, the integrals over the bottom surface, and over the far-field boundary vanish. The boundary integral of the second-order diffraction potential is then composed of the boundary integral over the body hull and the boundary integral over the free surface. The potential part of the excitation force is obtained by adding the second-order Froude-Krylov force and the second-order diffraction force.

The potential part of the difference- and sum-frequencies excitation forces, with the 6−DOF quadratic transfer function (QTF), $\boldsymbol{T}_{F_P}(\beta_1,\beta_2,\omega_1,\omega_2)$, is given as follows:

$$\boldsymbol{F}_{exc_2}^{(2)} = Re\left\{\boldsymbol{T}_{F_P}^{-}a_1a_2^*e^{-i(\omega_1-\omega_2)t}\right\} + Re\left\{\boldsymbol{T}_{F_P}^{+}a_1a_2e^{-i(\omega_1+\omega_2)t}\right\},$$

$$\boldsymbol{T}_{F_P}^{\pm} = \left[\boldsymbol{F}_{H_{I_1}}^{\pm} + \boldsymbol{F}_{H_{DB_1}}^{\pm} + \boldsymbol{F}_{H_{DF_1}}^{\pm} + \boldsymbol{F}_{H_{DF_2}}^{\pm}\right]/a_1a_2^{\mathcal{C}_\pm}, \tag{22}$$

where $\boldsymbol{F}_{H_{I_1}}^{\pm}$ is the Froude-Krylov force computed as in Eq. (18). The diffraction force is composed of several terms: the body forcing term, $\boldsymbol{F}_{H_{DB_1}}^{\pm}$, the free surface forcing term in the finite domain, $\boldsymbol{F}_{H_{DF_1}}^{\pm}$, and the asymptotic free surface forcing term in the infinite domain, $\boldsymbol{F}_{H_{DF_2}}^{\pm}$.

The diffraction force due to the body forcing terms is composed of i) the terms involving only the first derivatives, $\boldsymbol{F}_{H_{DB_{11}}}^{\pm}$, and ii) the second derivatives, $\boldsymbol{F}_{H_{DB_{12}}}^{\pm}$. The terms with second derivatives are expressed as a function of the first derivatives using the Green formulation. The force is then expressed as

$$\boldsymbol{F}_{H_{DB_1}}^{\pm} = \boldsymbol{F}_{H_{DB_{11}}}^{\pm} + \boldsymbol{F}_{H_{DB_{12}}}^{\pm} \tag{23}$$

$$\boldsymbol{F}_{H_{DB_{11}}}^{\pm} = i\omega^{\pm}\rho \iint_{S_{B_0}}\left(\partial_{\boldsymbol{n}}\Phi_I^{(2)\pm} - \frac{1}{2}\left[\begin{array}{l}\left(\dot{\boldsymbol{\varkappa}}_1^{(1)} - \nabla\Phi_1^{(1)}\right)\cdot R_2^{(1)\mathcal{C}_\pm}(\boldsymbol{n}_0) \\ +\left(\dot{\boldsymbol{\varkappa}}_2^{(1)\mathcal{C}_\pm} - \nabla\Phi_2^{(1)\mathcal{C}_\pm}\right)\cdot R_1^{(1)}(\boldsymbol{n}_0)\end{array}\right]_{S_{B_0}}\right)\boldsymbol{\psi}^{\pm}dS$$

$$\boldsymbol{F}_{H_{DB_{12}}}^{(2)\pm} = \frac{i\omega^{\pm}\rho}{2} \iint_{S_{B_0}}\left[\begin{array}{l}\left(\nabla\Phi_2^{(1)\mathcal{C}_\pm}\cdot\nabla\right)\left(\boldsymbol{\psi}^{\pm}\boldsymbol{\mathcal{X}}_1^{(1)}\right) + \left(\nabla\Phi_1^{(1)}\cdot\nabla\right)\left(\boldsymbol{\psi}^{\pm}\boldsymbol{\mathcal{X}}_2^{(1)\mathcal{C}_\pm}\right) \\ -\left(\nabla\cdot\left(\boldsymbol{\psi}^{\pm}\boldsymbol{\mathcal{X}}_1^{(1)}\right)\right)\nabla\Phi_2^{(1)\mathcal{C}_\pm} - \left(\nabla\cdot\left(\boldsymbol{\psi}^{\pm}\boldsymbol{\mathcal{X}}_2^{(1)\mathcal{C}_\pm}\right)\right)\nabla\Phi_1^{(1)}\end{array}\right]\cdot\boldsymbol{n}_0\, dS$$
$$- \frac{i\omega^{\pm}\rho}{2}\int_{\Gamma_0}\left[\left(\boldsymbol{\psi}^{\pm}\boldsymbol{\mathcal{X}}_1^{(1)}\right)\times\nabla\Phi_2^{(1)\mathcal{C}_\pm} + \left(\boldsymbol{\psi}^{\pm}\boldsymbol{\mathcal{X}}_2^{(1)\mathcal{C}_\pm}\right)\times\nabla\Phi_1^{(1)}\right]\cdot d\boldsymbol{\Gamma}.$$

where the segmented water-line, $d\boldsymbol{\Gamma} = (n_{0_2}, -n_{0_1}, 0)d\Gamma$.

The diffraction force due to the free-surface forcing over the finite domain S_{F_1}, $\boldsymbol{F}_{H_{DF_1}}^{(2)\pm}$, is calculated with the evaluated integrands on a user-input free-surface mesh with a circular boundary at radius $r = R_e$. The force is also composed of the terms in the first derivatives, $\boldsymbol{F}_{H_{DF_{11}}}^{\pm}$, and second derivatives, $\boldsymbol{F}_{H_{DF_{11}}}^{\pm}$. The second derivative terms are expressed with $\partial_z^2\Phi_I = k^2\Phi_I$ and $\partial_z^2\Phi_P \approx k^2\Phi_P$. The force is then expressed as

$$\boldsymbol{F}_{H_{DF_1}}^{\pm} = \boldsymbol{F}_{H_{DF_{11}}}^{\pm} + \boldsymbol{F}_{H_{DF_{12}}}^{\pm}, \tag{24}$$

$$\boldsymbol{F}^{\pm}_{H_{DF_{11}}} = \frac{i\omega^{\pm}\rho}{g} \iint_{S_{F_1}} \begin{bmatrix} i(\omega_1 \pm \omega_2)\left[\nabla\Phi^{(1)}_1 \cdot \nabla\Phi^{(1)\mathcal{C}_\pm}_{P_2} + \nabla\Phi^{(1)}_{P_1} \cdot \nabla\Phi^{(1)\mathcal{C}_\pm}_{I_2}\right] \\ -\frac{i\omega_1}{2g}\left[\Phi^{(1)}_1(-\omega_2^2\partial_z\Phi^{(1)\mathcal{C}_\pm}_{P_2}) + \Phi^{(1)}_{P_1}(-\omega_2^2\partial_z\Phi^{(1)\mathcal{C}_\pm}_{I_2})\right] \\ \mp\frac{i\omega_2}{2g}\left[\Phi^{(1)\mathcal{C}_\pm}_2(-\omega_1^2\partial_z\Phi^{(1)}_{P_1}) + \Phi^{(1)\mathcal{C}_\pm}_{P_2}(-\omega_1^2\partial_z\Phi^{(1)}_{I_1})\right] \end{bmatrix}_{z=0} \boldsymbol{\psi}^{\pm} dS$$

$$\boldsymbol{F}^{(2)\pm}_{H_{DF_{12}}} = \frac{i\omega^{\pm}\rho}{2g} \iint_{S_{F_1}} \begin{bmatrix} -\left(i\omega_1\Phi^{(1)}_1\right)k_2^2\Phi^{(1)\mathcal{C}_\pm}_{P_2} - \left(i\omega_1\Phi^{(1)}_{P_1}\right)k_2^2\Phi^{(1)\mathcal{C}_\pm}_{I_2} \\ \mp\left(i\omega_2\Phi^{(1)\mathcal{C}_\pm}_2\right)k_1^2\Phi^{(1)}_{P_1} \mp \left(i\omega_2\Phi^{(1)\mathcal{C}_\pm}_{P_2}\right)k_1^2\Phi^{(1)}_{I_1} \end{bmatrix} \boldsymbol{\psi}^{\pm} dS.$$

The diffraction force due to the free-surface forcing over the infinite domain is given as

$$\boldsymbol{F}^{\pm}_{H_{DF_2}} = \frac{i\omega^{\pm}\rho}{g}\left(\mathcal{K}^{\pm}_1(k_1,k_2,\omega_1,\omega_2)\left[\boldsymbol{I}^{\pm}_{DF_{11}} + \boldsymbol{I}^{\pm}_{DF_{12}}\right] + \mathcal{K}^{\pm}_2(k_1,k_2,\omega_1,\omega_2)\left[\boldsymbol{I}^{\pm}_{DF_{21}} + \boldsymbol{I}^{\pm}_{DF_{22}}\right]\right) \tag{25}$$

where

$$\mathcal{K}^{\pm}_1(k_1,k_2,\omega_1,\omega_2) = \mp i\omega^{\pm}k_1k_2$$

$$\mathcal{K}^{\pm}_2(k_1,k_2,\omega_1,\omega_2) = i\omega^{\pm}\frac{\Omega^2(k_1,D)}{g}\frac{\Omega^2(k_2,D)}{g} \mp \frac{i\omega_1\omega_2}{2}\left(\frac{k_1^2}{\omega_1\cosh^2(k_1D)} \pm \frac{k_2^2}{\omega_2\cosh^2(k_2D)}\right)$$

$$\boldsymbol{I}^{\pm}_{DF_{11}} = \int_0^{2\pi}\int_{R_e}^{\infty} \cos(\vartheta-\beta_1)\Phi^{(1)}_{I_1}\Phi^{(1)\mathcal{C}_\pm}_{P_2}\,\boldsymbol{\psi}^{\pm} r dr d\vartheta$$

$$\boldsymbol{I}^{\pm}_{DF_{12}} = \int_0^{2\pi}\int_{R_e}^{\infty} \cos(\vartheta-\beta_2)\Phi^{(1)}_{P_1}\Phi^{(1)\mathcal{C}_\pm}_{I_2}\,\boldsymbol{\psi}^{\pm} r dr d\vartheta$$

$$\boldsymbol{I}^{\pm}_{DF_{21}} = \int_0^{2\pi}\int_{R_e}^{\infty} \Phi^{(1)}_{I_1}\Phi^{(1)\mathcal{C}_\pm}_{P_2}\,\boldsymbol{\psi}^{\pm} r dr d\vartheta,\ \boldsymbol{I}^{\pm}_{DF_{22}} = \int_0^{2\pi}\int_{R_e}^{\infty} \Phi^{(1)}_{P_1}\Phi^{(1)\mathcal{C}_\pm}_{I_2}\,\boldsymbol{\psi}^{\pm} r dr d\vartheta$$

with the potentials expressed in asymptotic form as defined in [19, 20]. The potentials are the function of the vertical profile function,

$$\mathcal{F}(k,D,z) = \frac{1}{kD(1-\tanh^2 kD) + \tanh kD}\mathcal{Z}(k,D,z),$$

the perturbed or radiation Kochin functions with the coefficients (C_P, S_P, C_R, and S_R), the Bessel function of the first kind (J_l) and $\epsilon_0 = 0$, $\epsilon_l = 2$ for $l \geq 1$. The integrals can then be rewritten as

$$I^{\pm}_{DF_{11}} = \frac{-ia_1 g 8\pi\sqrt{k_2k^{\pm}}}{\omega_1}\mathcal{F}(k_2,D,0)\mathcal{F}(k^{\pm},D,0) \times \sum_{l=0}^{\infty}\frac{1}{2}I^{\pm}_{r^1_l}\left[I^{\pm}_{\vartheta^1_{l-1}} + I^{\pm}_{\vartheta^1_{l+1}}\right]$$

$$I^{\pm}_{DF_{12}} = \frac{\mp ia_2 g 8\pi\sqrt{k_1k^{\pm}}}{\omega_2}\mathcal{F}(k_1,D,0)\mathcal{F}(k^{\pm},D,0) \times \sum_{l=0}^{\infty}\frac{1}{2}I^{\pm}_{r^2_l}\left[I^{\pm}_{\vartheta^2_{l-1}} + I^{\pm}_{\vartheta^2_{l+1}}\right]$$

$$I^{\pm}_{DF_{21}} = \frac{-ia_1 g 8\pi\sqrt{k_2k^{\pm}}}{\omega_1}\mathcal{F}(k_2,D,0)\mathcal{F}(k^{\pm},D,0)\sum_{l=0}^{\infty}I^{\pm}_{r^1_l}I^{\pm}_{\vartheta^1_l}$$

$$I^{\pm}_{DF_{22}} = \frac{\mp ia_2 g 8\pi\sqrt{k_1k^{\pm}}}{\omega_2}\mathcal{F}(k_1,D,0)\mathcal{F}(k^{\pm},D,0)\sum_{l=0}^{\infty}I^{\pm}_{r^2_l}I^{\pm}_{\vartheta^2_l}$$

where

$$I^{-}_{r^1_l} = \int_{R_e}^{\infty} e^{i(k^- - k_2)r}\epsilon_l i^l J_l(k_1r)dr,$$

$$I^{+}_{r^1_l} = \int_{R_e}^{\infty} e^{i((k^+ + k_2)r + \pi/2)}\epsilon_l i^l J_l(k_1r)dr,$$

$$I^{\pm}_{\vartheta^1_l} = \int_0^{2\pi}\begin{bmatrix}\cos l(\vartheta-\beta_1) \\ \left(\sum_{m=0}^{\infty}C^{\mathcal{C}_\pm}_{mP_2}\cos m\vartheta + S^{\mathcal{C}_\pm}_{mP_2}\sin m\vartheta\right) \\ \left(\sum_{n=0}^{\infty}C^{\pm}_{nR}\cos n\vartheta + S^{\pm}_{nR}\sin n\vartheta\right)\end{bmatrix} d\vartheta,$$

$$I^{\pm}_{r^2_l} = \int_{R_e}^{\infty} e^{i((k^{\pm} + k_1)r + \pi/2)}\epsilon_l (i^l)^{\mathcal{C}_\pm} J_l(k_2r)dr,$$

$$I^{\pm}_{\vartheta^2_l} = \int_0^{2\pi}\begin{bmatrix}\cos l(\vartheta-\beta_2) \\ \left(\sum_{m=0}^{\infty}C_{mP_1}\cos m\vartheta + S_{mP_1}\sin m\vartheta\right) \\ \left(\sum_{n=0}^{\infty}C^{\pm}_{nR}\cos n\vartheta + S^{\pm}_{nR}\sin n\vartheta\right)\end{bmatrix} d\vartheta.$$

The integral over $\vartheta \in [0, 2\pi]$ can be obtained analytically. The integral over $r \in [R_e, \infty]$ is computed analytically for $r \in [0, \infty]$ subtracted by the numerical integration for $r \in [0, R_e]$.

3. Program documentation

This section describes the features of the main programs, their compilation, the procedure to run the programs, and test cases.

3.1. Main programs

Fig. 2 shows a global overview of the software. There are three main programs: a mesh preprocessor, NEMOH1, and NEMOH2. The program features are described as follows.

3.1.1. Mesh preprocessor

NEMOH mesh preprocessor, the executable file **`mesh`**, is used to generate the NEMOH mesh file with a given geometry input file and an input `Mesh.cal` file. This **`mesh`** is not a meshing code but allows the user to refine an existing mesh and to calculate properties such as displacement, buoyancy center, and hydrostatic stiffness. It also makes estimates of masses and the inertia matrix. The concept with this program is to write by hand a coarse description of the body under consideration in a `GeomInput` file and to have the **`mesh`** preprocessor make the refined mesh for the NEMOH calculations.

3.1.2. NEMOH1: 1st-order solver

NEMOH1 solves the first-order potential flow problem. There are four modules: **`preProc`**, **`hydrosCal`**, **`solver`** and **`postProc`**, described as follows.

- **`preProc`**: processes the input mesh file and generates the body condition for each calculation case (diffraction and radiation). The outputs are used as input for **`solver`**.
- **`hydrosCal`**: computes hydrostatic parameters, i.e. stiffness matrix and inertia matrix. The output file will be used in the **`postProc`** to compute the RAOs.
- **`solver`**: solves the boundary value problems for each problem, diffraction and radiation, defined in the file `Normalvelocities.dat`, provided by the **`preProc`**.

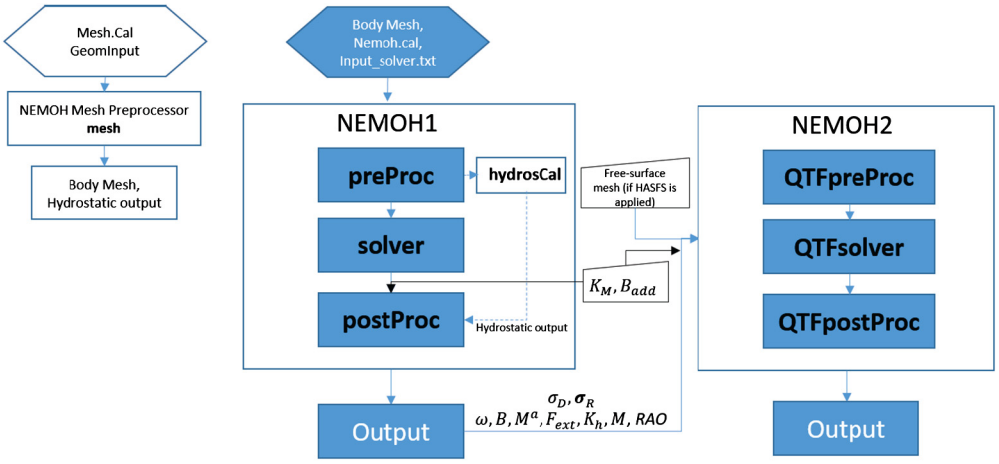

Fig. 2. Global flowchart of NEMOH software.

- **`postProc`**: post-processes the **`solver`**'s output files. The results are the excitation forces, added mass, and damping coefficients. Optionally, the program computes the impulse response functions of radiation damping and excitation force, the Kochin coefficient, the free-surface elevation, and the motion response amplitude operator.

3.1.3. NEMOH2: 2nd-order QTF module

NEMOH2 computes the second-order wave loads that are expressed as Quadratic Transfer Functions (QTF). There are three modules in this program: **`QTFpreProc`**, **`QTFsolver`** and **`QTFpostProc`**, described as follows

- **`QTFpreProc`**: computes the perturbed potential, the total potential, the normalized radiation potential, and the corresponding velocities on the body panels, the waterline, and the free-surface panels.
- **`QTFsolver`**: computes the quadratic part and the potential part of the second order loads.
- **`QTFpostProc`**: adds all the computed QTF parts and produces the total QTF.

3.2. Compilation

NEMOH uses two external libraries, BLAS and LAPACK, that have to be installed before the compilation. For the compilation, two tools are required; i) a Fortran compiler (*e.g.*, gfortran or ifort on Unix/Linux platforms), ii) a cross-platform tool, CMake, for building and testing the software package. The compilation produces all the executables for each module described above. The program can be compiled on any computer architecture. It has been tested on Windows and Unix/Linux platforms.

Note that the Gitlab releases provide pre-compiled executable files for Windows and Linux platforms.

3.3. Running NEMOH

NEMOH has been developed for command-line runs. Matlab wrapper files are also provided for running NEMOH in the Matlab environment. To run NEMOH, some input files have to be user-provided. Section 3.3.1 describes the required input files and also the output files. Test cases for verifying the NEMOH results are provided with the reference data from commercial BEM solvers such as AQUAPLUS (which is the ancestor of NEMOH) and HYDROSTAR [18], described in Section 3.3.2.

3.3.1. Input and output files

The following files are needed for the input; some depend on the user-specified choice in `Nemoh.cal`:

- `Nemoh.cal` contains all the NEMOH computation parameters
- `Mesh.cal` contains information about the `geomInput` file. It is an input for **`mesh`** and **`hydrosCal`**.
- a `meshfile`, input for **`preProc`**, or `geomInput` file, input for **`mesh`**
- `input_solver.txt` contains **`solver`** parameters
- `Km.dat` and `Badd.dat`, are the additional stiffness and damping matrices. These optional inputs are used for **`postProc`**/**`QTFpreProc`**
- `FSmeshfile` contains the free-surface mesh. This optional input serves to compute the total QTF, including the free-surface integral.

NEMOH produces the following main output files, some depending on the user-specified choice in `Nemoh.cal`,

- hydrostatic files: inertia and stiffness matrices,
- hydrodynamic coefficients: Froude-Krylov force, excitation force, added-mass, damping coefficient,
- pressure field on the body hull, Kochin function, free-surface elevation,
- motion Response Amplitude Operator (RAO),
- total difference- and sum-frequencies QTFs.

3.3.2. Test cases

There are 13 test cases, 8 test cases for NEMOH1 and 5 test cases for NEMOH2, provided in the software package. These test cases enable the user to test and verify all the features in NEMOH. The test cases cover: i) different body inputs, such as single body or double bodies, symmetrical or non-symmetrical body, ii) the different solver options, iii) the post-processing options, Kochin function and free-surface elevation, iv) with and without the removal of irregular frequencies, v) sum- and difference-frequencies QTFs, vi) uni- or bi-directional QTFs, vii) geometry complexities from a simple cylinder, a spar-buoy (OC3-HYWIND or Softwind) floating wind-turbine platform and an OC4-semisubmersible platform.

In the test cases, the NEMOH results can be compared with the reference data from AQUAPLUS and HYDROSTAR provided in the package. A Tecplot [28] layout file and Matlab [29] post-processing files are provided to ease the comparison.

A makefile is provided for running the test cases on the Unix/Linux environment. The test cases can also be run in the Matlab environment with an m-file, also provided.

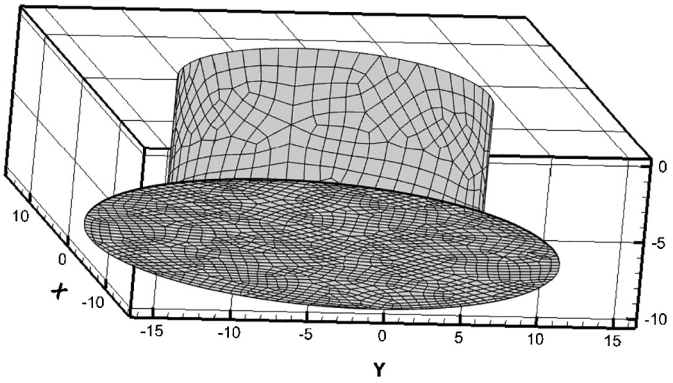

Fig. 3. Body boundary mesh for the truncated cylinder with thin heave plate.

4. Results

Extensive verification has been conducted for various geometries, presented in [19,20] and in the user manual [30].

This section presents the results obtained with NEMOH covering the first-order solution for a truncated cylinder with a thin heave plate, the first-order and second-order solutions for the SOFTWIND [31] spar-buoy platform and the OC4-semisubmersible [32] platform. Similar second-order results for the platforms with different wave directions have been reported in [20].

4.1. Description of test cases

The geometries and dimensions of the platforms are as follows. The first platform is the truncated cylinder with a thin heave plate. The cylinder has a draft of 10 m and a radius of 10 m, the heave plate has a thickness of 0.1 m and a radius of 15 m. The center of gravity is located at (0,0,-7.5) m. Second, the SOFTWIND platform has a draft of 91.4 m, a radius of 5.6 m on the upper part, and 9 m on the bottom part. The center of gravity is located at (0,0,-71.56) m. Third, the OC4 platform is configured with the main column, a radius of 3.25 m, a draft of 20 m, three columns with heave-plates, the upper columns with a radius of 6 m, a draft of 14 m, the base columns with a radius of 12 m, and a draft of 6 m below the upper columns. The center of gravity is considered at (0,0,0) m. Infinite water depth is considered for the first platform, and a water depth of 200 m is considered for the second and third platforms.

The floating platforms are discretized in quadrilateral panels using the open-source mesh generator, GMSH [33], as shown in Fig. 3-5. The truncated cylinder with a thin heave plate is discretized by 3464 panels including 262 lid panels, Fig. 3. The SOFTWIND platform is discretized by 1872 panels and the OC4 by 2196 panels. For the sum-frequency QTF computation with SOFTWIND, the free-surface integral terms are computed on an unstructured mesh with 8304 quadrilateral panels over a radius of 50 m, see Fig. 4. The choice of the number of panels is based on the convergence study of the first-order hydrodynamic coefficients. The convergence test results for the OC4 platform are shown in [19].

For the case of the truncated cylinder with a thin heave plate, only first-order computation is conducted with the frequency interval $[0, 4]$ rad/s with a frequency step of 0.2 rad/s. The first-order results for the softwind and OC4 platforms are computed with wave frequency interval in $[2\pi/100, 2\pi]$ rad/s with a frequency step set to $2\pi/100$ rad/s. The frequency interval is chosen such that in the QTF computation, the $\omega^{\pm}$ are in the range of the specified frequency interval otherwise an interpolation procedure will be applied in NEMOH. In this case, the frequency step is chosen to be related to the interested low-frequency motion, period 100 s. Zero-degree wave direction is considered for the SOFTWIND platform; 0 and 30 degrees wave directions are considered for the OC4 platform.

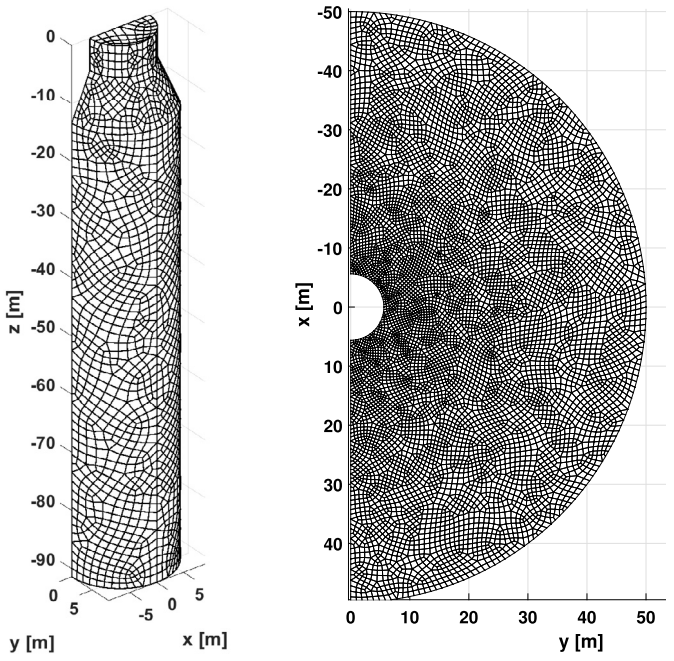

Fig. 4. Body boundary mesh (left) and free surface mesh (right) for the SOFTWIND platform.

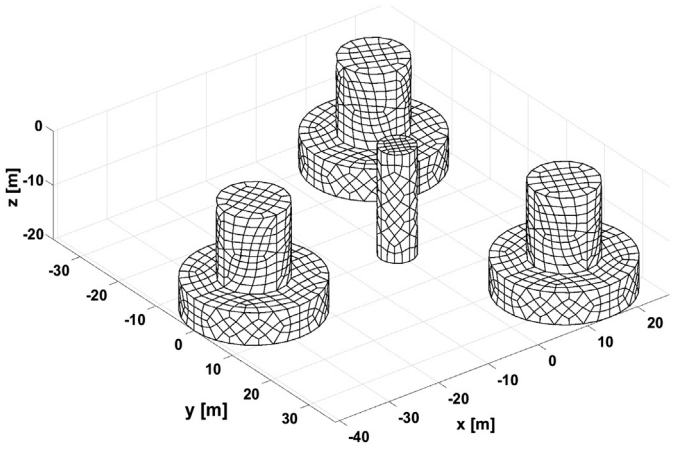

Fig. 5. Body boundary mesh for the OC4-platform.

For the QTFs, the results are shown for bi-chromatic waves with ω_1 and ω_2 in the interval $[2\pi/100, \pi]$ rad/s, uni-directional 0 degrees for the SOFTWIND case and bi-directional $\beta_1 = 30$ degrees and $\beta_2 = 0$ degree for the OC4 platform. For both floating platforms, the difference-frequency QTFs of the surge, heave, and pitch are computed without the free-surface integrals. The sum-frequency full QTFs, including the free-surface integrals, are computed for the SOFTWIND platform. In most of the applications, the free surface terms are negligible in the difference-frequency QTFs but are important for the sum-frequency QTFs [34,35].

The computed results of NEMOH are compared with the results obtained using one or more of the following commercial software, i) WAMIT [15], ii) DIODORE [22], iii) HYDROSTAR [18] developed by Bureau Veritas. The QTFs results are compared only with HYDROSTAR results. For a direct comparison with the different software, the same mesh is used in the computations.

The irregular frequency is applied in the computations of all the test cases except if it is mentioned as not applied. In NEMOH, the

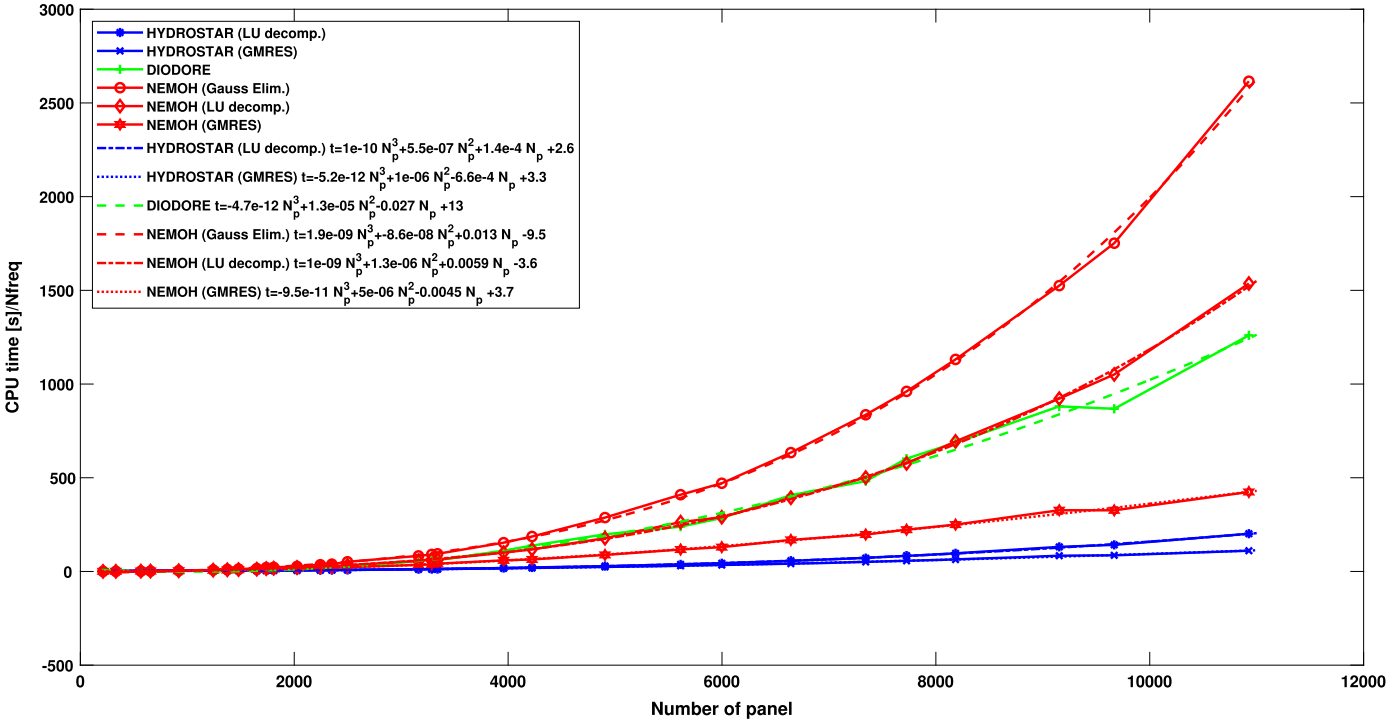

Fig. 6. Comparison of CPU time per one computed frequency between HYDROSTAR with LU decomposition and GMRES solvers, DIODORE, NEMOH with Gauss elimination, LU decomposition and GMRES solvers, and the corresponding regression plots.

irregular-frequencies removal method is applied with the extended boundary integral method and will be applied if the lid panels are included in the mesh file. In the other software, a similar irregular frequency removal method is applied with the software-generated waterplane lid panels.

Note that the software packages have different Green function models and implementations. For the QTFs computation, NEMOH and the other software have different approaches for the semi-infinite free surface integrals.

The following subsections describe the results of the first-order hydrodynamic coefficients and the second-order results (QTFs). The first-order results cover computations for enhanced computational efficiency, irregular frequency removal, the cylinder with a thin heave plate, and Softwind and OC4-Semisubmersible platforms

All the QTF results are normalized by ρg, where $\rho = 1025$ kg/m^3 and $g = 9.81$ m/s^2. The normalized QTF of forces and moments has unit N s^2/kg and N ms^2/kg, respectively.

4.2. First-order results

4.2.1. Enhanced computational efficiency

In the previous version of NEMOH, the Gauss-Elimination method was used to solve the linear system of the BIE, Eq. (8). In NEMOH v3.0, two more options for the linear system solver are available: LU-decomposition and GMRES-iterative solvers. These newly implemented solvers enhance the efficiency of the processing time (CPU).

To demonstrate the computational performance, several computations were conducted on a substructure of the OC4 platform, a column assembled with the heave plate, with 30 different numbers of panels starting from 212 panels to 10927 panels. The computations were set for one single wave frequency, 0.879 rad/s, 0-degree wave direction, water depth of 535 m, one diffraction problem, and 6 radiation problems. The computations were conducted for each solver and compared with those obtained using HYDROSTAR and DIODORE [22]. The computation was done without parallelization on a laptop with an Intel i7 processor and 32 GB RAM.

Fig. 6 shows the CPU time comparison between NEMOH with different solvers and with the other software packages. To solve a large system with more than 3000 panels, NEMOH with the GMRES solver is more effective than the other solvers. The CPU time for NEMOH with the LU-decomposition method is similar to that of DIODORE. The best computation performance is obtained by HYDROSTAR either with LU decomposition or with the GMRES solver. This may be due to a more efficient implementation of constructing the influence matrix.

4.2.2. Irregular frequency removal (IRR)

As described in Section 2.3.5, the extended BIE with the lid panels are applied to remove the irregular frequencies. The performance of this IRR method is shown in Fig. 7 for the added mass and damping coefficients of a substructure of the OC4 platform, a cylinder. NEMOH with the IRR method removes the irregular frequencies. The NEMOH results agree well with HYDROSTAR, except that the HYDROSTAR results still have irregularities at frequencies close to 4 rad/s.

4.2.3. Truncated cylinder with a thin heave plate

A thin heave plate in the truncated cylinder aims to enhance the performance of the structure motion in waves. The thin heave plate with a small displacement could significantly change the added mass, damping, excitation forces and thus the motion performance. However, as noted in [4,7] the thin heave plate is very challenging for boundary element methods when the distance of the source and flow points are very close. For the same structure, as shown in [7], NEMOH had poor performance compared to WAMIT and HAMS. An axisymmetric mesh is used and provided in [7]. It turns out that the axisymmetric mesh has panels with a high ratio of width and length at the center of the heave plate bottom. This gives inaccuracy in the NEMOH calculation.

To avoid the high aspect ratio panels, an unstructured mesh is generated as shown in Fig. 3. The same mesh is used for the computations using NEMOH, WAMIT, HYDROSTAR and DIODORE. In the computation of WAMIT and NEMOH v2, the irregular frequency re-

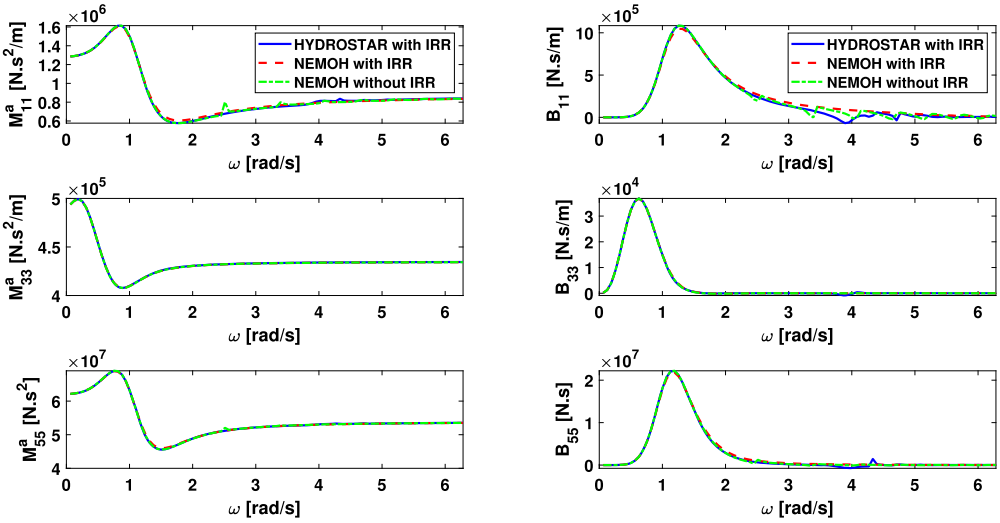

Fig. 7. Comparison of added mass (left) and damping coefficients (right) between HYDROSTAR with IRR (blue, solid line), NEMOH with IRR (red, dashed line), NEMOH without IRR (green, dash-dotted line) for the cylinder. (For interpretation of the colors in the figures, the reader is referred to the web version of this article.)

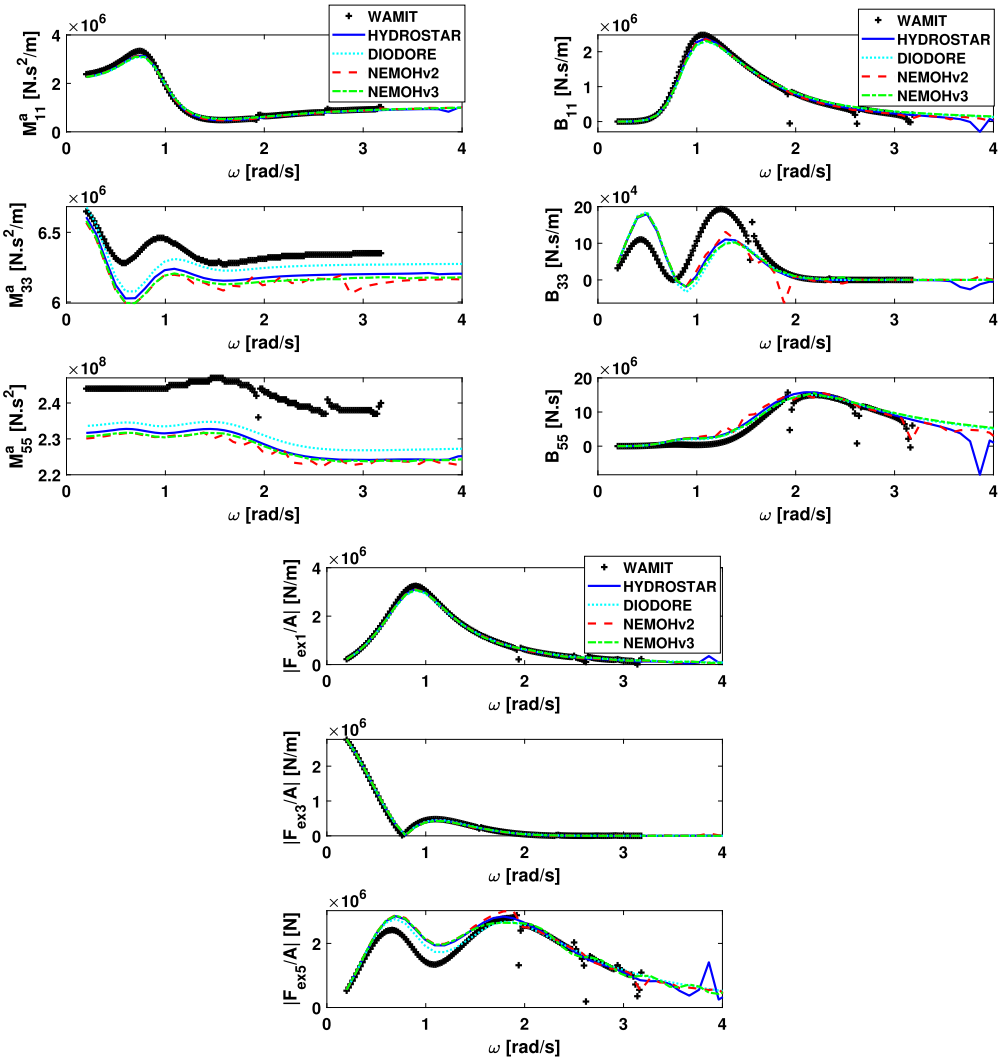

Fig. 8. Comparison of added mass (left top), damping coefficients (right top) and the excitation forces (bottom) between WAMIT without IRR (black, plus symbol), HYDROSTAR with IRR (blue, solid line), DIODORE with IRR (cyan, dotted line), NEMOH v2 without IRR (red, dashed line), NEMOH v3 with IRR (green, dash-dotted line) for the truncated cylinder with a thin heave plate.

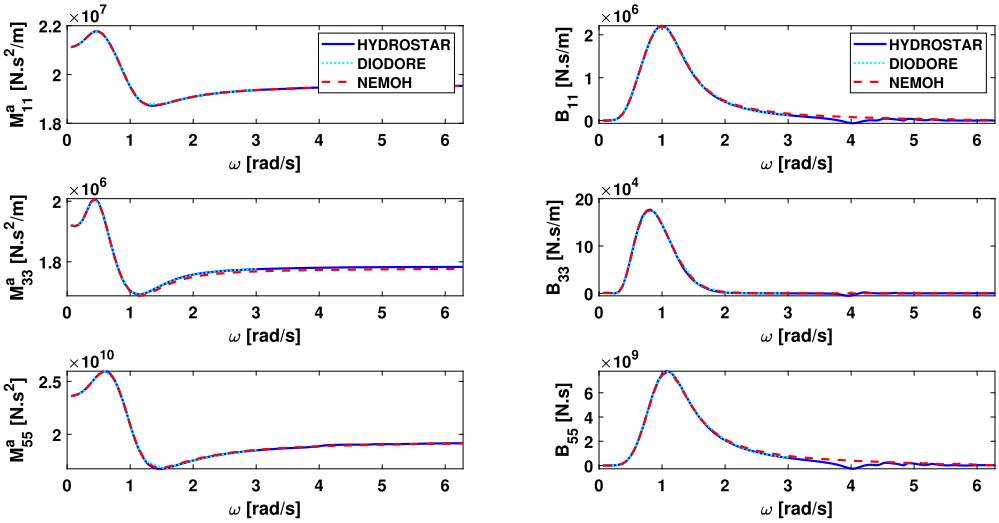

Fig. 9. Comparison of added mass (left) and damping coefficients (right) between HYDROSTAR (blue, solid line), DIODORE (cyan, dotted-line), and NEMOH (red, dashed line) for the SOFTWIND platform.

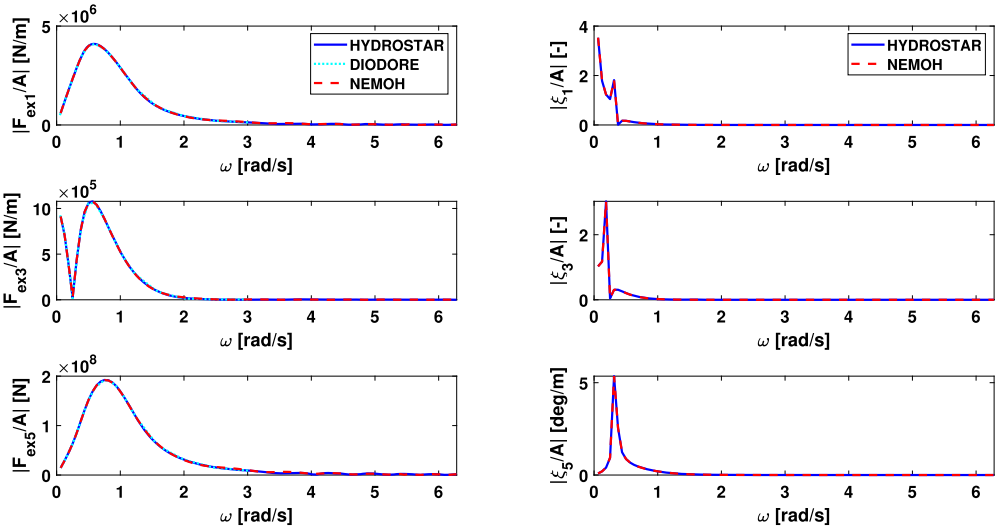

Fig. 10. Comparison of the response amplitude operator of excitation force (left) between HYDROSTAR (blue, solid line), DIODORE (cyan, dotted-line), and NEMOH (red, dashed line) for the SOFTWIND platform and of motion (right) between HYDROSTAR and NEMOH; the top, middle, and bottom rows are for surge, heave, and pitch, respectively.

moval method was not applied. The comparison of added mass, damping coefficient and excitation force in Fig. 8 shows that all the BEM codes perform quite well. NEMOH v3 gives slightly better results than NEMOH v2. The NEMOH results are very close to the HYDROSTAR and DIODORE results. The slight differences with WAMIT results are observed in the heave and pitch added masses, the heave damping coefficient and the pitch excitation force. Observe that, the HYDROSTAR results have irregular frequencies near $\omega = 4$ rad/s although the irregular frequency removal method was applied. Overall, the NEMOH results obtained here are much better than the corresponding results in [7].

4.2.4. Softwind and OC4-semisubmersible

The hydrodynamic coefficients, the added mass and damping coefficients, of the SOFTWIND platform are presented in Fig. 9. Fig. 10 shows the linear response amplitude operator of the excitation force and the motion of the platform. The heave excitation force shows the cancellation effect, $F_{exc} \approx 0$ N at $\omega = 0.25$ rad/s, due to the geometry tapering from the smallest radius to the largest radius, see Fig. 4.

The added mass and damping coefficients of the OC4-semisubmersible platform are shown in Fig. 11. The RAOs of the excitation forces are shown in Fig. 12 and the RAOs of the motions are shown in Fig. 13; the results are shown for the wave direction of 0 and 30 degrees.

As shown in the comparisons, NEMOH, DIODORE and HYDROSTAR are in excellent agreement. This verifies the first-order results of NEMOH against the commercial software. The only slight difference is the presence of an irregular frequency at $\omega = 4$ rad/s in the HYDROSTAR result for the SOFTWIND case.

4.3. Second-order results

4.3.1. Difference-frequency QTFs

Comparisons of the normalized magnitude of difference-frequency QTFs between HYDROSTAR and NEMOH are shown in the density plots, Fig. 14 for the SOFTWIND platform with wave direction $(\beta_1, \beta_2) = (0°, 0°)$ and in Fig. 16 for the OC4 platform with $(\beta_1, \beta_2) = (30°, 0°)$. The normalized magnitude QTFs are computed as $|\boldsymbol{T}^-_F|/\rho g$ where $\boldsymbol{T}^-_F = \boldsymbol{T}^-_{F_Q} + \boldsymbol{T}^-_{F_P}$, $\boldsymbol{T}^-_{F_Q}$ as in Eq. (20) and $\boldsymbol{T}^-_{F_P}$, Eq. (22), is approximated as $\boldsymbol{T}^-_{F_P} \approx \left[\boldsymbol{F}^{\pm}_{H_{l_1}} + \boldsymbol{F}^{\pm}_{H_{DB_1}}\right]/a_1 a_2^{\mathcal{C}_\pm}$. The dif-

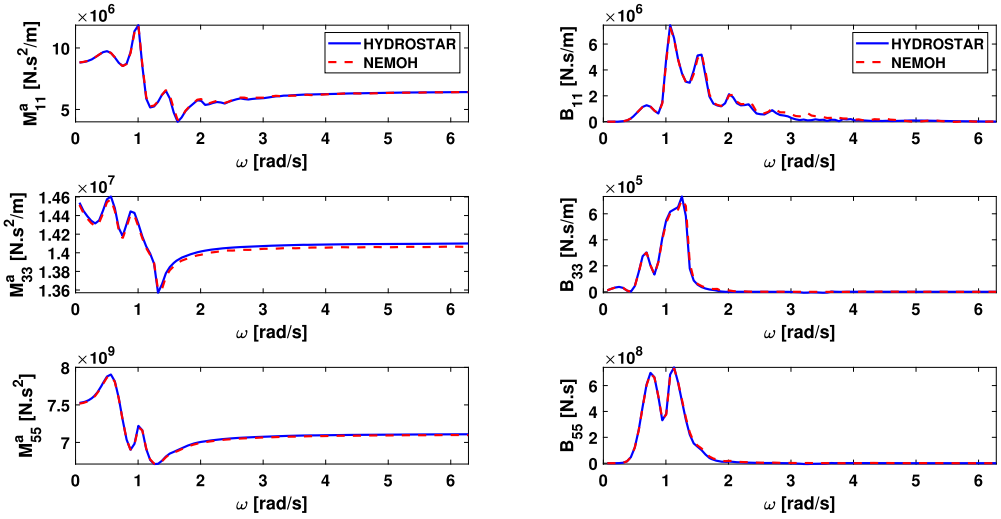

Fig. 11. Comparison of added mass (left) and damping coefficients (right) between HYDROSTAR (blue, solid line) and NEMOH (red, dashed line) for the OC4-semisubmersible platform.

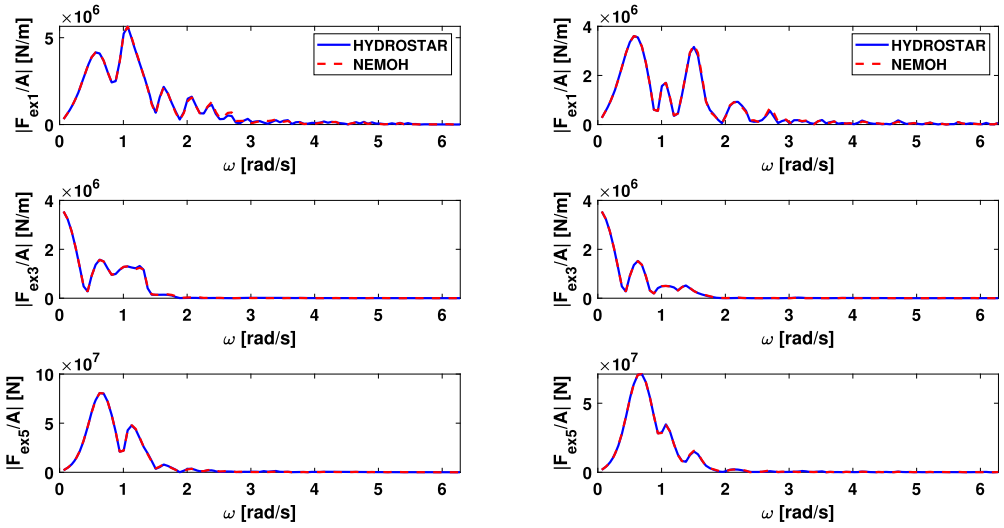

Fig. 12. Comparison of the response amplitude operator of excitation force for the wave directions 0 degrees (left) and 30 degrees (right) between HYDROSTAR (blue, solid line) and NEMOH (red, dashed line) for the OC4-semisubmersible platform; the top, middle, and bottom rows are for surge, heave, and pitch, respectively.

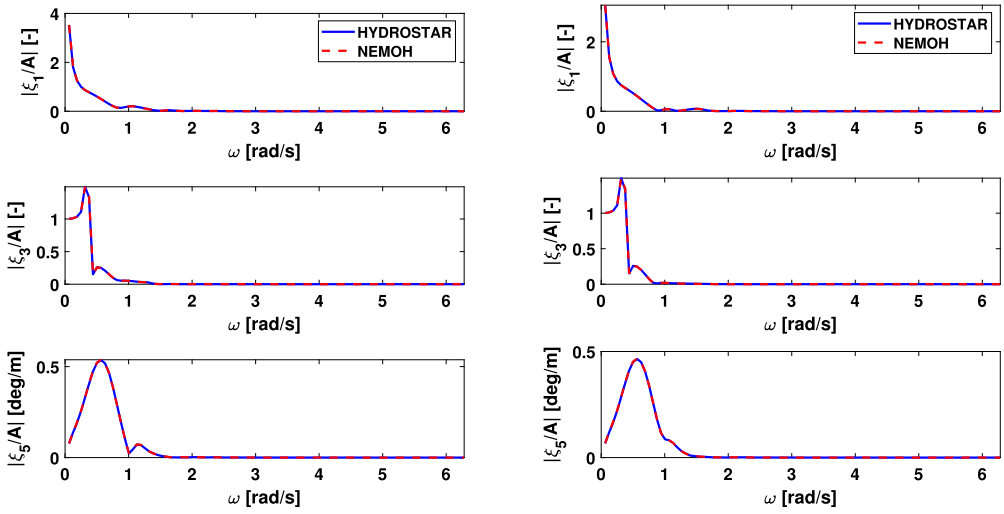

Fig. 13. Comparison of response amplitude operators of motion for the wave directions 0 degrees (left) and 30 degrees (right) between HYDROSTAR (blue, solid line) and NEMOH (red, dashed line) for the OC4-semisubmersible platform; the top, middle, and bottom rows are for surge, heave, and pitch, respectively.

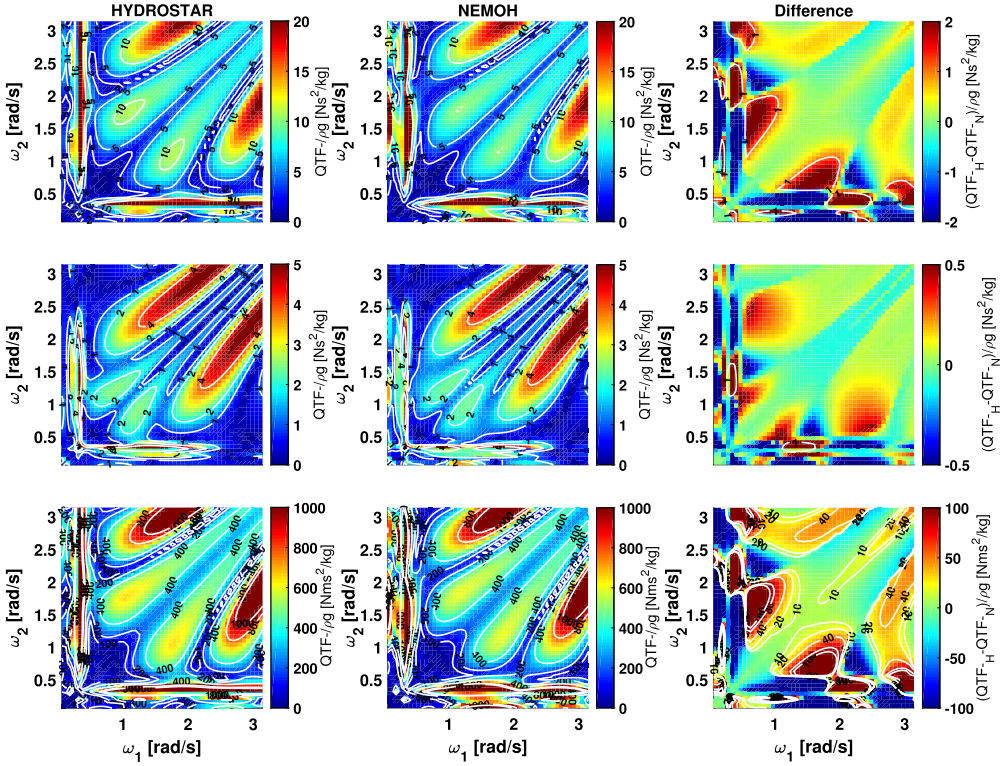

Fig. 14. Density plots of the normalized uni-directional, $(\beta_1, \beta_2) = (0°, 0°)$, surge difference frequency QTF magnitude (without the free-surface integrals) for the floating SOFTWIND platform; on the top, middle and bottom rows are for surge, heave, and pitch, respectively. HYDROSTAR results are on the left column, NEMOH results are on the middle column and the difference is on the right column.

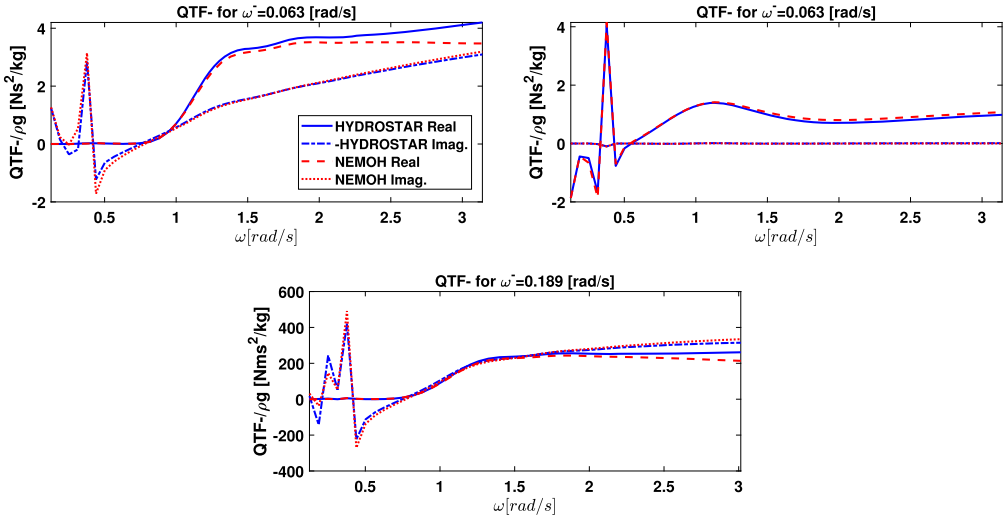

Fig. 15. Comparison of the off-diagonal uni-directional, $(\beta_1, \beta_2) = (0°, 0°)$, difference frequency QTF for the SOFTWIND platform between HYDROSTAR, real part (blue, solid-line), imaginary part (blue, dashed-dot line) and NEMOH, real part (red, dashed-line), imaginary part (red, dotted-line). Top-left is for surge, the top-right for heave (the first off-diagonal) and the bottom for pitch (the third off-diagonal).

ference in the QTF results between HYDROSTAR and NEMOH are quantified by $\left(|\boldsymbol{T}_F^-|_{HYDROSTAR} - |\boldsymbol{T}_F^-|_{NEMOH}\right)/\rho g$.

The results show that excellent agreement is achieved between the two programs, with quite a small difference, $< 10\%$ for all the motion modes, as shown in the plots for surge, heave, and pitch. Fig. 16 shows more complex density plots due to the complex interaction in the OC4 platform.

When computing QTFs, the off-diagonal QTFs are usually the most relevant information one is looking for, especially for the mooring design. The corresponding off-diagonal QTFs (real and imaginary parts) are shown for the SOFTWIND platform in Fig. 15 and for the OC4 in Fig. 17. The first off-diagonal QTFs are shown for the surge and heave motions, while for the pitch motion the third off-diagonal is shown. The ω^- on the first off-diagonal QTF is at the surge natural frequencies and the third off-diagonal QTF is at the pitch natural frequencies of the OC4 platform.

In the plots, it is shown that the radiation effect due to the body displacement is dominant in the frequency interval $\omega < 0.5$ rad/s, while the excitation effect is dominant in the other frequency interval $\omega > 0.5$ rad/s. Studying the off-diagonal difference-

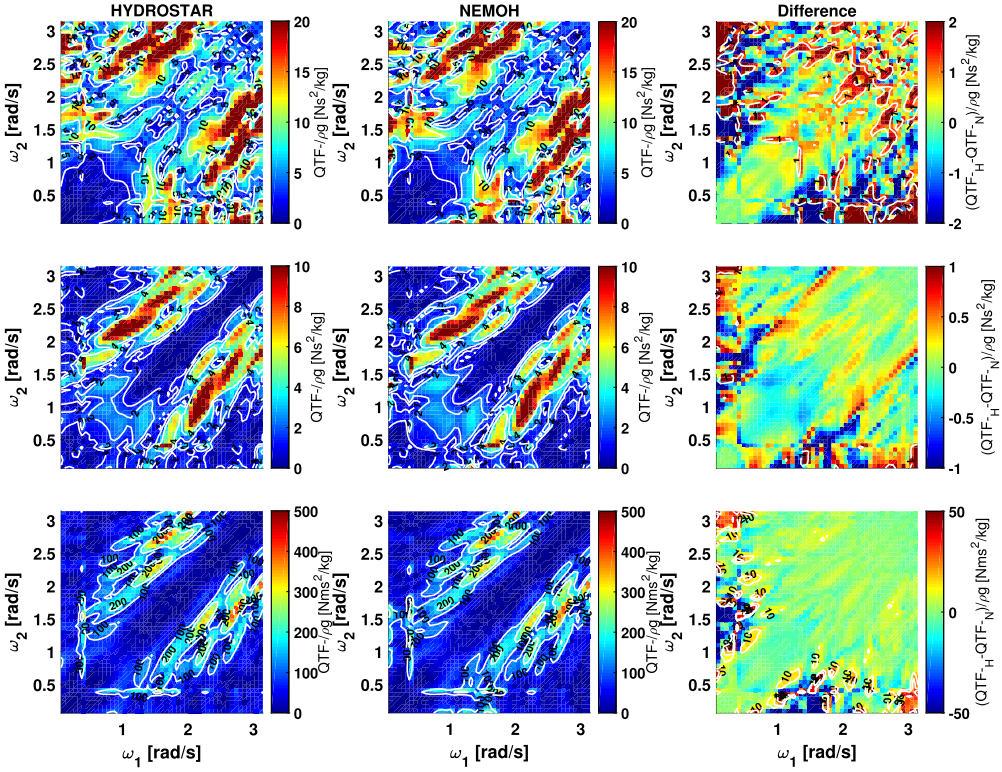

Fig. 16. Density plots of the normalized bi-directional, $(\beta_1, \beta_2) = (30°, 0°)$, surge difference frequency QTF magnitude (without the free-surface integrals) for the floating OC4-semisubmersible platform; on the top, middle and bottom rows are for surge, heave, and pitch, respectively. HYDROSTAR results are on the left column, NEMOH results are on the middle column and the difference is on the right column.

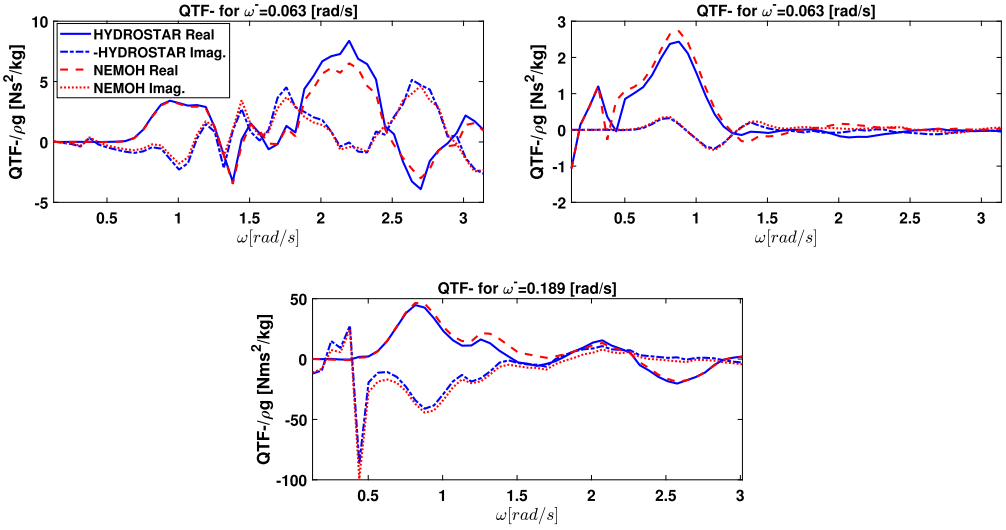

Fig. 17. Comparison of the off-diagonal bi-directional, $(\beta_1, \beta_2) = (30°, 0°)$, difference frequency QTF for the OC4-semisubmersible platform between HYDROSTAR, real part (blue, solid line), imaginary part (blue, dashed-dot line) and NEMOH, real part (red, dashed line), imaginary part (red, dotted line). Top-left is for surge, the top-right for heave (the first off-diagonal) and the bottom for pitch (the third off-diagonal).

frequency QTFs at the natural frequencies of the structure is important for understanding the low-frequency response of the floating structure.

Similar to the density plots comparison, the comparison plots of the off-diagonal QTFs between the two programs show that excellent agreement is also achieved. This verifies the difference-frequency QTF computation within NEMOH in the spar-buoy type SOFTWIND platform and a more complex structure such as the OC4-submersible platform.

4.3.2. Sum-frequency QTFs

A comparison of the sum-frequency full QTFs between the two programs is shown in the density plots, Fig. 18, and in the off-diagonal line plots, Fig. 19. The normalized magnitude of sum-frequency QTFs is computed as $|\boldsymbol{T}_F^+|/\rho g$, where $\boldsymbol{T}_F^+(0°, 0°, \omega_1, \omega_2) = \boldsymbol{T}_{F_Q}^+ + \boldsymbol{T}_{F_P}^+$, Eqs. (20) and (22). Good agreement is achieved, although in this case the irregular frequency removal method in NEMOH was switched off due to an issue with the computation of the potential on the free-surface mesh. An improvement in

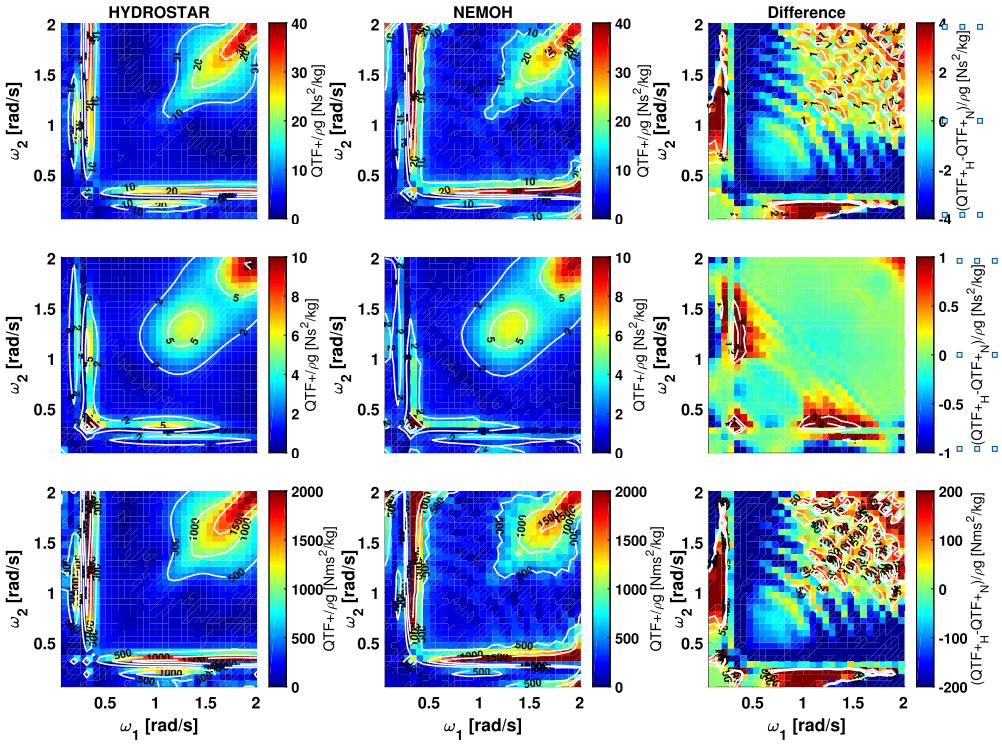

Fig. 18. Density plots of the normalized sum-frequency full QTF magnitude (including the free-surface integrals) for the floating SOFTWIND platform; the top, middle, and bottom rows are for surge, heave, and pitch, respectively. HYDROSTAR results are in the left column, NEMOH results are in the middle column and the difference plots are in the right column.

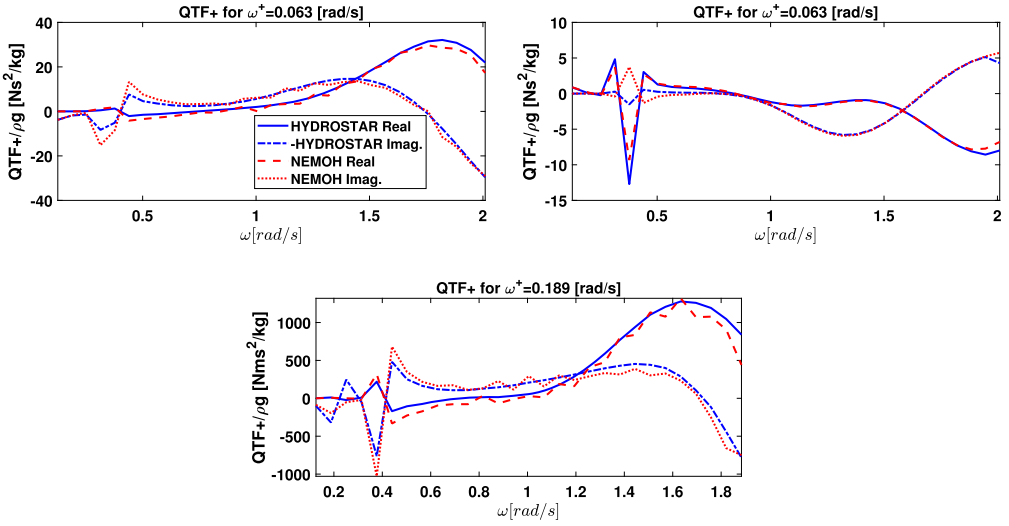

Fig. 19. Comparison of the off-diagonal sum-frequency full QTF for SOFTWIND platform between HYDROSTAR, real part (blue, solid line), imaginary part (blue, dashed-dot line) and NEMOH, real part (red, dashed line), imaginary part (red, dotted line). The top-left is for surge, the top-right for heave (the first off-diagonal) and the bottom for pitch (the third off-diagonal).

this part of NEMOH implementation will be added in the next release.

This verifies the full sum-frequency QTF computation (including the free surface integral) within NEMOH in the spar-buoy type SOFTWIND platform.

5. Conclusion

The NEMOH code was developed to compute first- and second-order wave loads on floating structures in the frequency domain. The first-order module has been used by many researchers and engineers in the ocean engineering community. This new release includes a new extension module for computing QTFs, and improvement in the first-order module, i.e. irregular frequency removal, and greater computation efficiency. The code has been shown to be accurate and efficient.

The NEMOH outputs can be used as input to a time-domain solver in order to estimate the dynamic response of a floating structure with the presence of moorings or a power take-off system. In the EU-funded FLOATECH[1] project on the development of an open-source QBlade-ocean, NEMOH outputs of the first- and

[1] www.floatech-project.com.

second-order hydrodynamic coefficients are used as input for the time-domain solver of the structural design of the floating offshore wind turbine software, QBlade.[2]

NEMOH is an open-source code, redistributed under the terms of the GNU General Public License (version 3) as published by the Free Software Foundation. Along with the source code, documentation [30] is provided which makes compilation and execution of the code easy. In addition, various test cases with reference data are provided in the software package to verify the results. To our knowledge, this NEMOH release will be the only open-source software that provides the QTF module.

Declaration of competing interest

The authors declare that they have no known competing financial interests or personal relationships that could have appeared to influence the work reported in this paper.

Data availability

Data will be made available on request.

Acknowledgement

This work was done within the framework of the FLOAT-ECH project. This project has received funding from the European Union's Horizon 2020 research and innovation program under grant agreement No 101007142.

We thank Moran Charlou from LHEEA, ECN for his help in finalizing the NEMOH v3.0 release in Gitlab. We thank Dr. W. Sheng from Lancaster University for providing the WAMIT computation results of the truncated cylinder with a thin heave plate. We are grateful to the reviewers for their useful suggestions.

Appendix A. Supplementary material

Supplementary material related to this article can be found online at https://doi.org/10.1016/j.cpc.2023.108885.

References

[1] G. Remery, A. Hermans, Soc. Pet. Eng. J. 12 (03) (1972) 191–198, https://doi.org/10.2118/3423-PA.
[2] J. Pinkster, Soc. Pet. Eng. J. 15 (06) (1975) 487–494, https://doi.org/10.2118/4837-PA.
[3] C. Petrauskas, S. Liu, in: OTC Offshore Technology Conference, 1987, oTC-5458-MS.
[4] A. Babarit, G. Delhommeau, in: Proceedings of the 11th European Wave and Tidal Energy Conference, 2015.
[5] M. Penalba, T. Kelly, J.V. Ringwood, in: The 12th European Wave and Tidal Energy Conference at Cork, Ireland, 2017.
[6] P. Schmitt, C. Windt, J. Nicholson, B. Elsässer, Eur. J. Mech. B, Fluids 58 (2016) 9–19.
[7] W. Sheng, E. Tapoglou, X. Ma, C. Taylor, R. Dorrell, D. Parsons, G. Aggidis, Ocean Eng. 249 (2022) 110878.
[8] B. Yang, S. Wu, H. Zhang, B. Liu, H. Shu, J. Shan, Y. Ren, W. Yao, Renew. Sustain. Energy Rev. 167 (2022) 112668.
[9] L. da Silva, M. de Oliveira, B. Cazzolato, N. Sergiienko, G. Amaral, B. Ding, Ocean Eng. 261 (2022) 112033.
[10] C.E. Høeg, Z. Zhang, Ocean Eng. 266 (2022) 112952.
[11] D.M. Skene, N. Sergiienko, B. Ding, B. Cazzolato, Energies 14 (21) (2021).
[12] L. da Silva, N. Sergiienko, B. Cazzolato, B. Ding, Renew. Energy 199 (2022) 1424–1439.
[13] A. Combourieu, M. Lawson, A. Babarit, K. Ruehl, A. Roy, R. Costello, P. Laporte-Weywada, H. Bailey, in: Proceedings of the 11th European Wave and Tidal Energy Conference, 2015.
[14] G. Verao Fernández, V. Stratigaki, P. Troch, Energies 12 (3) (2019), https://doi.org/10.3390/en12030538, https://www.mdpi.com/1996-1073/12/3/538.
[15] WAMIT Inc, WAMIT, software program, https://www.wamit.com/.
[16] Y. Liu, in: Proceedings of the 14th European Wave and Tidal Energy Conference, Plymouth, UK, 2021.
[17] M. Philippe, A. Combourieu, C. Peyrard, F. Robaux, G. Delhommeau, A. Babarit, in: Proceedings of the 11th European Wave and Tidal Energy Conference, 2015.
[18] Bureau Veritas, HYDROSTAR Software v8.14, 2020.
[19] R. Kurnia, G. Ducrozet, J.-C. Gilloteaux, in: International Conference on Offshore Mechanics and Arctic Engineering, in: Ocean Engineering, vol. 5A, 2022, v05AT06A019.
[20] R. Kurnia, G. Ducrozet, in: 18èmes Journées de l'Hydrodynamique, 2022.
[21] LHEEA, NEMOH Software v3.0, Ecole Centreale Nantes, France, 2022, https://gitlab.com/lheea/Nemoh.
[22] Principia, DIODORE Software v5.5.2, 2021.
[23] B. Molin, Appl. Ocean Res. 1 (4) (1979) 197–202.
[24] X.-B. Chen, Etudes des réponses du second ordre d'une structure soumise à une houle aléatoire, PhD Thesis, Université de Nantes, 1988.
[25] G. Delhommeau, in: Proc. of 2nd Journées de L'hydrodynamique, 1989.
[26] V. Frayssé, L. Giraud, S. Gratton, J. Langou, A set of gmres routines for real and complex arithmetics on high performance computers, Tech. Rep. TR/PA/03/3, CERFACS, 2003, https://www.cerfacs.fr/algor/Softs/.
[27] š. Malenica, X.-B. Chen, Int. J. Offshore Polar Eng. 8 (02) (1998).
[28] Tecplot, software program, https://www.tecplot.com/.
[29] Matlab, software program, https://www.mathworks.com/products/matlab.html.
[30] R. Kurnia, G. Ducrozet, NEMOH v. 3.0: User Manual, Tech. Rep., LHEEA Lab, Ecole Centrale de Nantes, France, 2022.
[31] V. Leroy, S. Delacroix, A. Merrien, E. Bachynski-Polić, J.-C. Gilloteaux, Ocean Eng. 255 (2022) 111430.
[32] A. Robertson, J. Jonkman, M. Masciola, H. Song, A. Goupee, A. Coulling, C. Luan, Definition of the Semisubmersible Floating System for Phase II of OC4, Tech. Rep., National Renewable Energy Lab. (NREL), Golden, CO (United States), 2014.
[33] C. Geuzaine, J.-F. Remacle, GMSH Software v4.8.4, 2021.
[34] X. Chen, B. Molin, F. Petitjean, Mar. Struct. 8 (5) (1995) 501–524, moored and Tethered Structures.
[35] C. Monroy, G. de Hauteclocque, X.-B. Chen, A Practical $O(\Delta\omega)$ Approximation of Low Frequency Wave Loads, Offshore Technology of International Conference on Offshore Mechanics and Arctic Engineering, vol. 1, 2013.

[2] www.qblade.org.